Draft version August 31, 2016
Preprint typeset using LaTeX style emulateapj v. 5/2/11

arXiv:1608.01763v2 [astro-ph.CO] 30 Aug 2016

# ELUCID - EXPLORING THE LOCAL UNIVERSE WITH RECONSTRUCTED INITIAL DENSITY FIELD III: CONSTRAINED SIMULATION IN THE SDSS VOLUME

Huiyuan Wang[1], H.J. Mo[2,3], Xiaohu Yang[4,5], Youcai Zhang[6], JingJing Shi[1,7], Y. P. Jing[4,5], Chengze Liu[4], Shijie Li[4], Xi Kang[8] and Yang Gao[9]

*Draft version August 31, 2016*

## ABSTRACT

A method we developed recently for the reconstruction of the initial density field in the nearby Universe is applied to the Sloan Digital Sky Survey Data Release 7. A high-resolution N-body constrained simulation (CS) of the reconstructed initial condition, with $3072^3$ particles evolved in a $500h^{-1}$Mpc box, is carried out and analyzed in terms of the statistical properties of the final density field and its relation with the distribution of SDSS galaxies. We find that the statistical properties of the cosmic web and the halo populations are accurately reproduced in the CS. The galaxy density field is strongly correlated with the CS density field, with a bias that depend on both galaxy luminosity and color. Our further investigations show that the CS provides robust quantities describing the environments within which the observed galaxies and galaxy systems reside. Cosmic variance is greatly reduced in the CS so that the statistical uncertainties can be controlled effectively even for samples of small volumes.

*Subject headings:* dark matter - large-scale structure of the universe - galaxies: halos - methods: statistical

## 1. INTRODUCTION

One of the major aims of modern astrophysics is to understand how galaxies and galaxy systems form and evolve in the cosmic density field. In the current standard cosmogony, galaxies are assumed to form via radiative cooling and collapse of baryonic gas within the gravitational potentials of the dark matter structures (e.g. White & Rees 1978). Therefore exploring the relationships and interactions between baryonic gas, galaxies and dark matter is not only essential for understanding galaxy formation (e.g. Mo, van den Bosch & White 2010), but also important for using galaxies as tracers of the large-scale structure of the universe to test models for cosmology and dark matter particles (e.g., Peebles 1980; Peebles & Nusser 2010; Frenk & White 2012).

Many observational programs have been carried out to study the properties of galaxies and the baryonic gas, such as the intergalactic medium (IGM), circum-galactic medium (CGM) and interstellar medium (ISM). Galaxy properties are observed through multi-band galaxy surveys, such as the Sloan Digital Sky Survey (SDSS; York et al. 2000) and the Two Micron All Sky Survey (Skrutskie et al. 2006). The gas components can be detected via various ways, such as X-ray observations (e.g. Rosati et al. 2002), quasar absorption line systems (e.g. Danforth & Shull 2008), the 21 cm emission of neutral hydrogen gas (e.g., Koribalski et al. 2004), and millimeter/submillimeter emissions of molecular gas (e.g. Young et al. 1995). These observations provide unprecedented data base to study the processes that shape the eco-systems of galaxies we observe.

Theoretically, great progress has been made in understanding the structures in cold dark matter distribution (e.g. Zel'dovich 1970; Davis et al. 1985; Springel et al. 2005). The key concept in the buildup of the cosmic structure is the formation of dark matter halos, which are the hosts of galaxies. With the help of N-body simulations, the properties of the halo population, such as the spatial clustering, mass function, assembly history, and internal structure, are well understood (e.g. Mo et al. 2010 for a review). Within the current ΛCDM paradigm, methods, such as hydrodynamical simulations (Katz 1992; Navarro & White 1993; Vogelsberger et al. 2014; Schaye et al. 2015), semi-analytic model (White & Frenk 1991; Croton et al. 2006; Lu et al. 2011), and empirical models (Jing et al. 1998; Peacock & Smith 2000; Yang et al. 2003; Kravtsov et al. 2004; Zheng et al. 2005; Vale & Ostriker 2006; van den Bosch et al. 2007; Behroozi et al. 2010; Lu et al 2014), have been developed to understand how galaxies form and evolve in dark matter halos. However our understanding of the physical processes driving galaxy formation and evolution is still poor, and many competing models have been proposed.

It is, therefore, crucial to develop an optimal strategy that can sufficiently utilize the abundant observational data to constrain theoretical models. One promising way in this direction is to reconstruct the initial density field from which the observed universe has evolved, so that we can carry out simulations for the observed structures un-

[1] Key Laboratory for Research in Galaxies and Cosmology, Department of Astronomy, University of Science and Technology of China, Hefei, Anhui 230026, China; whywang@mail.ustc.edu.cn
[2] Department of Astronomy, University of Massachusetts, Amherst MA 01003-9305, USA
[3] Astronomy Department and Center for Astrophysics, Tsinghua University, Beijing 10084, China
[4] Center for Astronomy and Astrophysics, Shanghai Jiao Tong University, Shanghai 200240, China
[5] IFSA Collaborative Innovation Center, Shanghai Jiao Tong University, Shanghai 200240, China
[6] Key Laboratory for Research in Galaxies and Cosmology, Shanghai Astronomical Observatory, Nandan Road 80, Shanghai 200030, China
[7] SISSA, Via Bonomea 265, I-34136 Trieste, Italy
[8] Purple Mountain Observatory, the Partner Group of MPI für Astronomie, 2 West Beijing Road, Nanjing 210008, China
[9] The Computer Network Information Center of the Chinese Academy of Sciences, Beijing 100190, China

der various model assumptions. Such an approach makes it possible to compare model predictions with data in a way that is free of the cosmic variance produced by large-scale environments. This is particularly important when the observational samples are small, so the cosmic variance is a serious issue, as is the case for dwarf galaxies and for low-$z$ quasar absorption line systems. Moreover, accurate constrained simulations can also be used to study the histories and environments of real galaxies, as well as to investigate the interactions among galaxies, gas and dark matter.

There have been a lot of efforts in developing methods to reconstruct the initial conditions of the local universe (e.g. Peebles 1989; Hoffman & Ribak 1991; Nusser & Dekel 1992; Klypin et al. 2003; Brenier et al. 2003; Lavaux 2010; Jasche & Wandelt 2013; Kitaura 2013; Doumler et al. 2013; Wang et al. 2013; 2014; Sorce et al. 2016). These methods differ primarily in three ways. The first is the observational data that are used to constrain the reconstruction. Some of the previous investigations use galaxies as tracers of the cosmological density field, while others use the peculiar velocities of galaxies. With the advent of large redshift surveys, millions of galaxies now have accurate measurements for their positions, redshifts and intrinsic properties. Using galaxy distribution to trace the cosmic density field is an obvious choice. However, one long-standing problem is that galaxies are biased tracers of cosmic density, and the bias is not easy to model as it depends on how galaxies form in the cosmic density field. In the gravitational instability scenario of structure formation, the peculiar velocities are directly related to the mass density field. However, only a small fraction of nearby galaxies have reliable peculiar velocity measurements (e.g. Willick et al. 1997; Tully et al. 2013). More recently, halos represented by galaxy groups (e.g. Yang et al. 2005; 2007) have been used to reconstruct the current mass density field (Wang et al. 2009;2013; Muñoz-Cuartas et al. 2011), that can also serve as the base of the reconstruction. This method follows the spirit of current halo model (e.g. Cooray & Sheth 2002), and automatically takes into account the halo bias. The second difference is in the dynamical model used to predict the final density field from the initial conditions. A number of dynamical models have been used, including linear theory, Zel'dovich approximation and its modification (Nusser & Dekel 1992; Wang et al. 2013; Doumler et al. 2013; Sorce et al. 2016), second-order Lagrangian perturbation theory and its modifications (Jasche & Wandelt 2013; Kitaura 2013; Heß et al. 2013), and Particle-Mesh (PM) dynamics (Wang et al. 2014). The third difference is in the model used to infer the initial conditions from the observational constraints. Some of the previous investigations adopted backward models which evolve the present-day density/velocity fields back in time to the linear regime (Nusser & Dekel 1992; Doumler et al. 2013; Sorce et al. 2016). Recently, forward models are proposed, which use a probability distribution function consisting of a Gaussian prior and a likelihood function, and use MCMC-like algorithms to obtain the posterior of the initial density field (Jasche & Wandelt 2013; Kitaura 2013; Wang et al. 2013; 2014). Both the forward and backward models have their shortcomings: the backward models are only valid on scales where the multi-streaming (shell crossing) is absent, while the forward models require a large amount of computations to sample the parameter space. We refer the reader to Wang et al. (2014) for a more detailed discussion of the various methods.

In our first ELUCID paper (Wang et al. 2014, hereafter Paper I), we developed a forward method which employs the Hamiltonian Markov Chain Monte Carlo (HMC) algorithm to sample the posterior and uses the PM dynamics to evolve the initial condition to the present day. The reliability and accuracy of the HMC method were examined in great detail in Paper I and Wang et al. (2013) using simulations and mock catalogs constructed from them. In the second paper (Tweed et al. 2016 in preparation), we use $N$-body simulations to examine the reliability of the HMC method in reproducing the dark matter halo population. We found that our method can effectively trace massive halos back to the initial condition, which demonstrates that our reconstructed initial conditions can be used to simulate the formation histories of individual massive halos.

As the third in a series, this paper presents the application of method to the SDSS data. The paper is organized as follows. Section 2 describes briefly the method and observational data we use. Section 3 presents the statistical properties of our constrained simulation. The relations of the mass density field in the constrained simulation with the SDSS groups and galaxies are investigated in Section 4. Some interesting structures in the cosmic web as revealed by the constrained simulation are presented Section 5. Finally, we summarize our results and make further discussions some in Section 6.

## 2. DATA AND RECONSTRUCTION METHOD

In this section, we present a brief introduction to our reconstruction method developed in our early studies (Yang et al. 2005;2007; Wang et al. 2009;2012;2013; Paper I). The method starts from a redshift catalog of galaxies, such as the SDSS. First, we employ the halo-based group finder to identify galaxy groups from the galaxy catalog. Second, a model based on linear perturbation theory is applied to predict the peculiar velocity of each halo, and to correct the redshift to obtain its distance. Third, the groups in "real space" are used to reconstruct the present-day density field in the local Universe. Finally, we employ a HMC+PM method we have developed to reconstruct the initial conditions of the density field in the local Universe, and use $N$-body simulations to evolve the reconstructed initial conditions to obtain the formation history of the local Universe.

### 2.1. *SDSS galaxies and groups*

The galaxy sample used here is formed from the New York University Value-Added Galaxy Catalogue (Blanton et al. 2005) of the SDSS DR7 (Abazajian et al. 2009), but includes a set of improved reductions (see Yang et al. 2007). We select all galaxies in the main galaxy sample, with $r$-band apparent magnitudes $\leq 17.72$ after correcting for Galactic extinction, with redshifts in the range $0.01 \leqslant z \leqslant 0.2$, and with redshift completeness $C > 0.7$. Galaxy groups are identified by using the adaptive halo-based group finder developed by Yang et al. (2005; 2007). Group masses are estimated using abundance matching based on the ranking of a characteristic luminosity/stellar mass defined for each of the

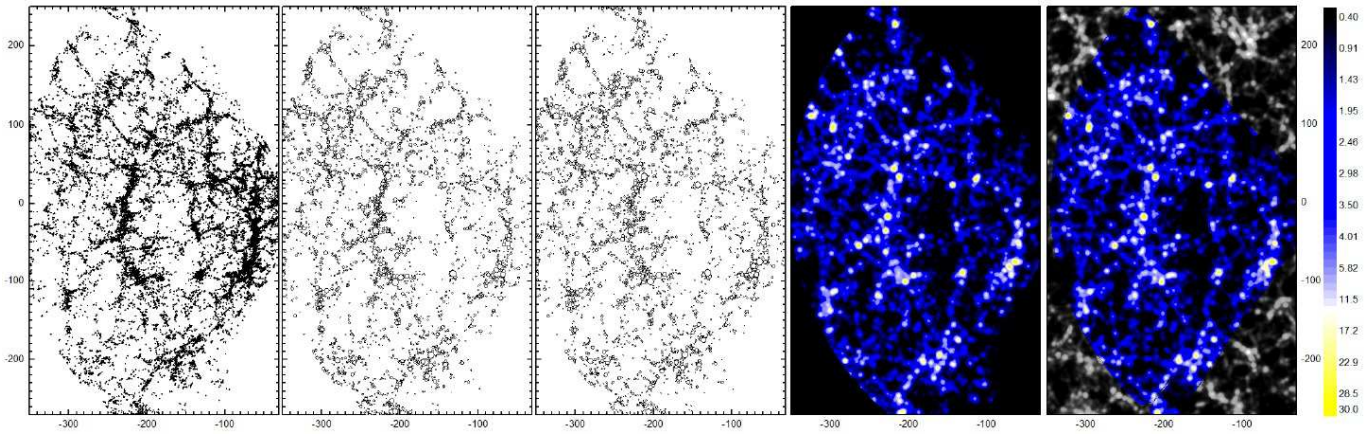


FIG. 1.— Galaxy, Group and Mass distributions in a $10\,h^{-1}$Mpc thick slice containing the Sloan Great Wall. First panel: galaxy distribution; Second panel: group distribution, the sizes of groups are scaled with their virial radii; Third panel: group distribution after correcting for redshift distortion; Fourth panel: projected mass density field of local Universe reconstructed from the group catalog; Fifth panel: projected mass density field obtained from constrained simulation at $z = 0$, and the color-coded region is the reconstruction volume. The density fields in the two right panels are smoothed with a Gaussian kernel with a radius of $2.0\,h^{-1}$Mpc and scaled with the mean density of the universe. The corresponding values of the densities are indicated by the color bar.

groups. Here, we adopt their luminosity-based group masses. Tests based on detailed mock catalogs suggest that more than 90% of the true halos can be identified and the fraction is even higher at the low and high mass ends. The uncertainties in the group mass estimation is about 0.35 dex for groups in the intermediate mass range, and 0.2 dex for both low and high mass groups (see Yang et al. 2007 for details).

The SDSS DR7 covers a sky area of 7,748 deg$^2$, consisting of two parts: a larger region in the Northern Galactic Cap (NGC) and a smaller region in the Southern Galactic Cap (SGC). In order to obtain a reliable reconstruction, we only use the more contiguous NGC region, which has a sky coverage of 7047 deg$^2$. As shown in Yang et al. (2007), the mass assignment based on the characteristic luminosity is complete to $z \sim 0.12$ for groups with mass $M_{\rm gr} \gtrsim 10^{12}\,h^{-1}{\rm M}_\odot$. In the following, we only use groups with $M_{\rm gr} \geq M_{\rm th} = 10^{12}\,h^{-1}{\rm M}_\odot$, so our reconstruction is restricted to the redshift range $0.01 \leq z \leq 0.12$, which will be referred to as the survey volume. Within the survey volume, the total number of groups with masses above $M_{\rm th}$ is 121,922.

The left two panels of Figure 1 show the spatial distributions of the galaxies and groups of $M_{\rm gr} \geq M_{\rm th}$ in a slice of $10\,h^{-1}$Mpc in thickness. The slice is chosen so that a large scale structure, called the Sloan Great Wall (Gott et al. 2005), is located at the center. One can see that there are lots of stick-like structures in the high density regions of the galaxy distribution, which point towards to the earth, which are the 'Fingers of God' (FOG) caused by the virial motions of galaxies within galaxy clusters. Such a FOG effect is largely mitigated in the distribution of groups, since the group finder takes into account the virial motions when assigning galaxies into groups. The reader is referred to Yang et al. (2007) for the details about the group catalog construction and halo mass estimation. Here we adopt the WMAP5 cosmology (Dunkley et al. 2009), instead WMAP3 adopted in the original Yang et al. (2007) paper. This mean all quantities are updated with this new cosmology.

### 2.2. *Correction for redshift distortion*

Since the method (shown in Section 2.3) used to reconstruct present-day density field from dark matter halos is designed to work, and has been tested in great detail, only in real space, we need to correct for redshift distortion in the distribution of groups in order to reconstruct the the present-day density field in real space from groups. In addition to the virial motion within groups, the large-scale bulk motions of groups can also produce redshift distortion (Kaiser 1987). To this end, we use the method developed in Wang et al. (2009; 2012). The basic idea is to apply the linear theory to the mass density field represented by groups to predict the peculiar velocity of each group, and then use it to correct for the redshift distortion. Since the procedure starts from groups in redshift space, iterations are required. Our tests suggest that two iterations are sufficient to achieve convergence. Of course, the linear theory is invalid on small scales; in particular it may predict too high bulk velocities around high density regions, such as clusters of galaxies. To reduce errors caused by this, the group mass density field is smoothed using a Gaussian kernel with a relatively large scale, corresponding to a mass of $\log(M_{\rm s}/\,h^{-1}{\rm M}_\odot) = 14.75$ at the mean density. The distribution of groups in "real space" is shown in the third panel of Figure 1. Our detailed tests based on mock group catalog showed that the mean offset between the predicted and original positions of groups is between 1.1 and $1.4\,h^{-1}{\rm Mpc}/h$ in the inner region of the survey volume (Wang et al. 2012; 2013). Such spatial offset corresponds to a velocity of $\sim 130\,{\rm km\,s^{-1}}$ according to Hubble law, which is similar to the typical uncertainty in the predicted velocities (e.g. Wang et al. 2009). In locations close to the boundary, the predicted velocities become more inaccurate, because velocity field is sensitive to large scale structures that are not well samples near the boundary.

### 2.3. *Reconstructing the present-day density field*

The group catalog in real space described above is used to reconstruct the present-day mass density field in the local Universe, using a method that closely follows the

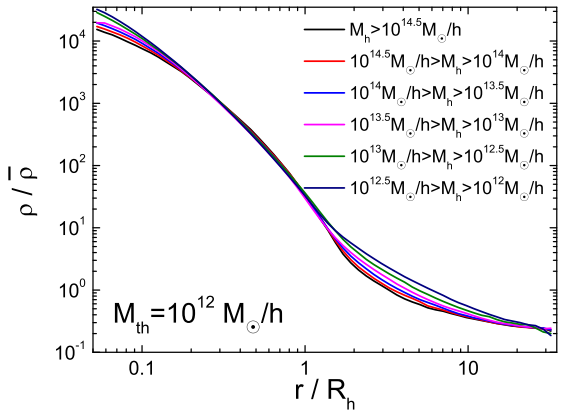


FIG. 2.— Density profile around halos in domain for halos in different mass bins, estimated from simulations

halo-domain reconstruction method developed in Wang et al. (2009; 2013). This method "convolve" the dark halo population (as represented by individual groups) with certain density profiles to reconstruction the large scale density field. These density profiles are obtained from 8 $N$-body simulations[10] of the WMAP5 cosmology using Gadget-2 code (Springel 2005). Following Wang et al. (2009), we partition each simulation box into a set of domains. Each domain contains one and only one halo with mass of $M_{\rm h} \geq M_{\rm th}$. The domain geometry of a halo is determined in such a way that any point in the domain is closer, based on a specific distance proximity, to the halo than to any other halo. The distance proximity between a point and a halo is defined as $r/R_{\rm h}$, where $r$ is the distance between them and $R_{\rm h}$ is the virial radius of the halo. We then calculate the average density profile around halos of the same mass in their corresponding domains. Figure 2 shows the results in six different mass bins. The eight simulations yield almost identical density profiles; we thus only show the results averaged over them.

The density field is then reconstructed in the following way. For a SDSS group, we pick a density profile according to its halo mass. A Monte Carlo technique is used to put particles around this group to sample the chosen density profile in the three dimensional space within its domain. This procedure is repeated for all the groups with masses above $M_{\rm th}$. Eventually, we get a present-day density field in the local Universe, which we denote by $\rho'_{\rm hd}(\mathbf{x})$. In Wang et al. (2009), the method was applied to dark halos extracted directly from $N$-body simulations. There it was found that the reconstructed density field correlates with the original simulated density field [denoted as $\rho_{\rm si}(\mathbf{x})$] extremely tightly. Wang et al. also applied the method to mock group catalogs to examine its reliability against uncertainties arising from false identification of groups and redshift distortion effects (Wang et al. 2013). It was found that, on scales of $\sim 3\,h^{-1}$Mpc, the root mean square (r.m.s) of $[\rho_{\rm si}(\mathbf{x}) - \rho'_{\rm hd}(\mathbf{x})]/\rho'_{\rm hd}(\mathbf{x})$ is between 0.3 and 0.5, corresponding to a scatter between 0.11 and 0.18 dex. These tests demonstrate that our method can reliably recover the density field from groups constructed from a galaxy redshift survey.

However, there is a small but systematical bias in the power spectra of the reconstructed density fields, as demonstrated in Wang et al. (2009). When the method was applied to halos extracted from $N$-body simulations, the power spectra of the reconstructed density fields, $P_{\rm hd}(k)$, were found to be 10%-20% lower than those of the original simulations, $P_{\rm sim}(k)$, on some scales. This loss of power is due to the fact that we have ignored the contribution of smaller halos and that the non-spherical nature of the structures on halo and larger scale is not accurately modeled by the density profiles, such as those shown in Figure 2. The ratio between these power spectra is about the same for all simulations. Thus, we can correct for the bias simply by using a correcting function defined as, $C_{\rm p}(k) = \sqrt{P_{\rm sim}(k)/P_{\rm hd}(k)}$. In practice we proceed in the following way. We embed $\rho'_{\rm hd}(\mathbf{x})$ in a periodic box of size $L_{\rm cs} = 500\,h^{-1}$Mpc, which is divided into $N_{\rm c} = 500$ grid cells in each dimension. For the grid cells inside the survey volume, we obtain the over-density, $\delta'_{\rm hd}(\mathbf{x}) = (\rho'_{\rm hd}(\mathbf{x}) - \bar{\rho})/\bar{\rho}$, where $\bar{\rho}$ is the mean density within the survey volume. For grid cells outside the survey volume, $\delta'_{\rm hd}(\mathbf{x})$ is set to zero. We then Fourier transform $\delta'_{\rm hd}(\mathbf{x})$ and multiply the resulting Fourier modes by $C_{\rm p}(k)$. Finally, we obtain the over-density field ($\delta_{\rm hd}(\mathbf{x})$ ) by the inverse Fourier transformation, and the densities are obtained through $\rho_{\rm hd}(\mathbf{x}) = (\delta_{\rm hd}(\mathbf{x}) + 1)\bar{\rho}$. In the forth panel of Figure 1, we show the reconstructed density field smoothed by using a Gaussian kernel of radius $R_{\rm s} = 2\,h^{-1}$Mpc. One can see that this density field matches well the distributions of both the galaxies and groups. In the following, we denote this reconstructed present-day density field by $\rho_{\rm hd}$.

In Appendix, we use realistic galaxy and group mock catalogs to further test our halo-domain method. We also estimate the uncertainties of the reconstruction by comparing the reconstruction and the original used to construct the mock catalog. We find that $\rho_{\rm hd}$ is strongly correlated with the density field of the original simulation, $\rho_{\rm si}$, without any significant bias. The typical scatter between the two densities, in terms of the r.m.s of $\log(\rho_{\rm hd}/\rho_{\rm si})$, are 0.09 and 0.20 dex at $R_{\rm s} = 4$ and $2\,h^{-1}$Mpc respectively. Moreover, we find that implementing the correction function improves the reconstruction at low density regions but has no significant effect on high density regions.

### 2.4. *Reconstructing the initial density field*

The HMC method (Wang et al. 2013; Paper I) is then employed to reconstruct the initial density field from the halo-domain density field. This method infers a linear density field in Fourier space, $\delta(\mathbf{k})$, from a posterior probability distribution function,

$$Q(\delta_j(\mathbf{k})|\rho_{\rm hd}(\mathbf{x})) = {\rm e}^{-\chi^2} \times G(\delta(\mathbf{k})) = {\rm e}^{-\sum_{\mathbf{x}}[\rho_{\rm mod}(\mathbf{x})-\rho_{\rm hd}(\mathbf{x})]^2\omega(\mathbf{x})/2\sigma^2_{\rm hd}(\mathbf{x})} \times \prod_{\mathbf{k}}^{\rm half}\prod_{j={\rm re}}^{\rm im}\frac{1}{[\pi P_{\rm lin}(k)]^{1/2}}{\rm e}^{-[\delta_j(\mathbf{k})]^2/P_{\rm lin}(k)}, \quad (1)$$

[10] Four of them use $512^3$ particles to trace the evolution of the cosmic density field in a cubic box with a side length of $300\,h^{-1}$Mpc, and four use $512^3$ particles in a smaller, $100\,h^{-1}$Mpc, box.

The second term, $G(\delta(\mathbf{k}))$, is the prior term that ensures $\delta(\mathbf{k})$ to have a Gaussian distribution with a given linear power spectrum, $P_{\rm lin}(k)$. The likelihood term, $e^{-\chi^2}$, is designed to ensure that the predicted density field ($\rho_{\rm mod}$) evolved from $\delta(\mathbf{k})$ according to a given structure formation model matches the input nonlinear density field, which in our case is the halo-domain density field $\rho_{\rm hd}$. In our application, $\sigma_{\rm hd}(\mathbf{x})$ is set to $0.5\rho_{\rm hd}(\mathbf{x})$, and the weighting function, $\omega(\mathbf{x})$, is specified below.

Since the input final density field is highly non-linear (Figure 1), it requires the structure formation model that links $\delta(\mathbf{k})$ and $\rho_{\rm mod}(\mathbf{x})$ to be sufficiently accurate so as to properly handle highly nonlinear dynamics on small scale. As shown in Paper I, an inaccurate model can introduce spurious non-Gaussian features in the reconstructed linear density field, which in turn can lead to significant bias in the predicted halo population. In this paper, we will follow Paper I and use the Particle-Mesh (PM) dynamics to follow the evolution of the density field. The PM scheme is often used to calculate the forces on large-scales in cosmological simulations. It can describe the structure formation and evolution accurately as long as the available computational resources allow the implementation with sufficiently high resolutions in both space and time. In what follows, reconstruction method based on the HMC with PM dynamics is referred to as the HMC+PM method.

Some important parameters used in the HMC and PM have to be specified before using the HMC+PM method to reconstruct the initial density field. As discussed in the previous section, the halo-domain density field is embedded in a $500\,h^{-1}$Mpc cubic box and the box is divided into $500^3$ grid cells, so that the grid cell size is $l_{\rm c} = 1\,h^{-1}$Mpc. For such a spatial resolution, twenty PM time steps are sufficient (see Paper I for detailed discussions). Since we perform the reconstruction in a very large volume, a more accurate PM model (equivalent to higher spatial resolution) will require computational resources that are beyond our reach at the moment. We note, however, that the PM model with $l_{\rm c} = 1\,h^{-1}$Mpc and 20 time steps is already much more accurate than any other structure formation models used so far in the literature for initial density field reconstruction, such as the Zel'dovich approximation and higher-order Lagrangian perturbation theory. With such a PM, significant discrepancies are still present on small scales between the model prediction and the fully non-linear density field, due to the inaccuracy of the model. The tests in Paper I suggest that smoothing both the density fields on a scale of $\geq 3l_{\rm c}$ can effectively eliminate such discrepancies. Here, we choose a more conservative smoothing scale of $4l_{\rm c} = 4\,h^{-1}$Mpc.

Another important parameter is the weighting function $\omega(\mathbf{x})$, which specifies the window in which the comparisons between $\rho_{\rm mod}$ and $\rho_{\rm hd}$ are to be made. In our reconstruction, all grids outside of the survey volume are assigned a zero weight, but not all grids inside the survey volume are assigned a full weight. Recall that the halo-domain density field, $\rho_{\rm hd}$, is smoothed on $R_{\rm s} = 4\,h^{-1}$Mpc in the HMC run. When performing the smoothing, the density outside of the survey volume is set to the mean cosmic density. It thus introduces uncertainties into $\rho_{\rm hd}$ at locations close to the boundary of survey volume. To

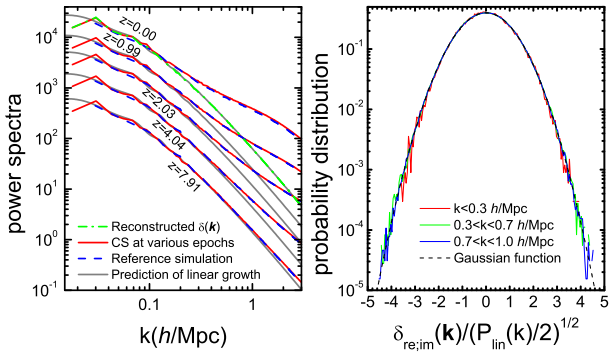


FIG. 3.— Left panel: the power spectra of the reconstructed linear density field (green dash-dotted line) and from the constrained simulation at various epochs (red solid lines). We also show the analytical linear power spectrum (grey lines) and those of the reference simulation (blue dashed lines) for comparison. Right panel: the probability distributions of the real and imaginary parts of the reconstructed linear density field, normalized by the linear power spectrum, at three different wavenumbers as indicated in the panel. The dashed line shows the expected Gaussian distribution.

deal with this boundary effect, we define a factor $f_{\rm c}(R_{\rm b})$ to characterize the closeness of a grid to the boundary. For a grid cell in the survey volume, $f_{\rm c}$ is the fraction of a spherical volume of radius $R_{\rm b}$ centered on the grid that is contained by the survey volume. Here we choose $R_{\rm b} = 10\,h^{-1}$Mpc, and use $f_{\rm c}(10\,h^{-1}{\rm Mpc}) = 0.84$ to define a boundary layer. When the curvature radius of the boundary surface is much larger than $10\,h^{-1}$Mpc (which is the case for most of the cases), $f_{\rm c} = 0.84$ corresponds to distance of $\sim 5\,h^{-1}$Mpc from the boundary, which is larger than the adopted smoothing scale. So the boundary effect can be ignored for all the grids with $f_{\rm c}(10\,h^{-1}{\rm Mpc}) > 0.84$. Such grids are assigned a weight of unity, while the grids with $f_{\rm c}(10\,h^{-1}{\rm Mpc}) \leq 0.84$ are assigned a weight of zero. The final volume (reconstruction volume hereafter) is about $2.73 \times 10^7 (\,h^{-1}{\rm Mpc})^3$, about 12% smaller than the original survey volume. Other parameters used in the HMC are set to be the same as in Paper I, and will not be repeated here.

Our HMC+PM makes calculations of a total 3000 HMC steps. The HMC system evolves quickly at the beginning, and achieves a convergent state after about 600 HMC steps. The typical scatter between $\rho_{\rm mod}$ and $\rho_{\rm hd}$ [hereafter TS, defined as the r.m.s of $\log(\rho_{\rm mod}/\rho_{\rm hd})$] after the 1000th step remains around 0.015 dex, indicating that after convergence the model density field match the input constraint very well. After convergence, the statistical properties of $\delta(\mathbf{k})$ remain similar, so we only show the results at the 1500th step. The green dash-dotted line in the left panel of Figure 3 shows the power spectrum of $\delta(\mathbf{k})$ at the 1500th HMC step, which is in good agreement with the theoretical power spectrum used in the model. The right panel shows the probability distributions of the real and imaginary parts of $\delta(\mathbf{k})$ for three different wave-numbers. These distributions closely match a Gaussian distribution, demonstrating that our method recovers the Gaussian property of the linear density field very well.

### 2.5. *The constrained simulation*

The linear density field output at the 1500th step is chosen to set up the initial condition for an $N$-body simulation. The initial condition is sampled with $3072^3$ dark matter particles at an initial redshift of $z_{\rm ini} = 100$. The mass of each particle is $3.09 \times 10^8\, h^{-1}{\rm M}_\odot$. Because the HMC process only generates the Fourier models at $k \leq N_{\rm c}\pi/L_{\rm cs}$, the missing modes at larger $k$ are complemented by assigning random phases. The density field is then evolved to present day using L-GADGET, a memory-optimized version of GADGET-2 (Springel et al. 2005). One hundred snapshots from $z = 19$ to $z = 0$ are produced, with the expansion factor evenly spaced in logarithmic space between successive snapshots. The simulation obtained this way is referred to as the constrained simulation (hereafter CS) in the following.

In the fifth panel of Figure 1, we show the present-day density field of the constrained simulation, $\rho_{\rm cs}$. Within the reconstruction volume, almost all large-scale structures, and even some small structures, are well recovered. The typical scatter (TS) between $\rho_{\rm hd}$ and $\rho_{\rm cs}$ is 0.018 dex when smoothed on a scale of $R_{\rm s} = 4\,h^{-1}$Mpc, only slightly larger than the TS between $\rho_{\rm hd}$ and $\rho_{\rm mod}$. When the densities are smoothed on $2\,h^{-1}$Mpc, the TS increases to about 0.13 dex. Given the large dynamical range in density involved, about 2 orders of magnitude, this relatively low TS indicates that $\rho_{\rm cs}$ matches $\rho_{\rm hd}$ well even on scales down to $\sim 2\,h^{-1}$Mpc. Note, however, the scatter discussed here only represents the uncertainties arising from the HMC+PM method; it does not include uncertainties caused by the other parts of the reconstruction discussed above. To estimate the full uncertainties of the constrained simulation, we have applied the reconstruction method to a realistic galaxy mock catalog (see Appendix). The TS between $\rho_{\rm cs}$ and the true density $\rho_{\rm si}$ are 0.10 and 0.23 dex for $R_{\rm s} = 4\,h^{-1}$Mpc and $2\,h^{-1}$Mpc, respectively. Recall that the TS between $\rho_{\rm hd}$ and $\rho_{\rm si}$ are 0.09 dex and 0.20 dex for the two values of $R_{\rm s}$, respectively. This suggests that the major sources of the uncertainties are from the inaccuracies of the redshift-distortion correction, group finder, and halo-domain reconstruction. See the Appendix for detailed discussions.

## 3. GENERAL STATISTICAL PROPERTIES OF CONSTRAINED SIMULATION

In this section, we present some statistical properties of the constrained simulation. When necessary, the results obtained from an $N$-body simulation with random initial phases are used for comparisons. The reference simulation assumes the same cosmology as our constrained simulation and its density field is traced by $1024^3$ particles in a cubic box of $300\,h^{-1}$Mpc on a side.

Power spectra are often used to measure the mass clustering and to characterize the large scale structure. In Figure 3 the power spectrum of the reconstructed linear density field is shown together with the power spectra of the constrained simulation (CS) at five different redshifts. The power spectra predicted by the linear perturbation theory and those of the reference simulation are also shown for comparison. As one can see, at the linear scales ($k < 0.15\,h{\rm Mpc}^{-1}$), the CS power spectra match the linear spectra very well. At smaller scales, the CS power spectra are significantly higher than the linear spectra, and the difference increases with the decreasing redshift, clearly owing to non-linear evolutions of the density field. However, these CS spectra match with those of the reference simulation almost perfectly, suggesting that the constrained simulation reproduces well the large scale structures statistically.

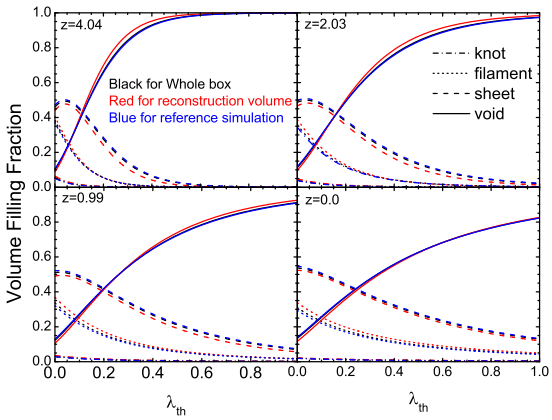


FIG. 4.— The fractions of volume classified as knots (dot-dashed lines), filaments (dotted lines), sheets (dashed lines) and voids (solid lines) as a function of the threshold $\lambda_{\rm th}$ at four different redshifts.

Since morphology of the cosmic web is complicated (Figure 1), the power spectrum alone is not sufficient to completely characterize a cosmic density field. Recently, much effort has been giving to developing methods to classify the cosmic web (e.g. Hahn et al. 2007; Lavaux & Wandelt 2010; Hoffman et al . 2012; Leclercq et al. 2016). Here we employ a dynamical classification, first developed by Hahn et al. (2007) and refined by Forero-Romero et al. (2009). The basic idea is to use the eigenvalues of the tidal tensor (or deformation tensor) to define the type of the local structure in a cosmic web. The tidal tensor, $\mathcal{T}_{ij}$, is defined as

$$\mathcal{T}_{ij} = \partial_i \partial_j \phi\,, \tag{2}$$

where, $\phi$ is the peculiar gravitational potential and can be calculated from the CS density perturbation ($\delta_{\rm cs}$) through a modified Poisson equation:

$$\nabla^2 \phi = \delta_{\rm cs}\,. \tag{3}$$

Note that this equation is scaled by $4\pi G\bar{\rho}$ and $\delta_{\rm cs}$ is defined over gird cells and smoothed on a comoving scale of $2\,h^{-1}$Mpc. We derive the three eigenvalues of the tidal tensor, $\lambda_1 \geq \lambda_2 \geq \lambda_3$, at each grid point, and classify a grid point by counting the number of eigenvalues above a given threshold $\lambda_{\rm th}$. A knot point corresponds to all the three eigenvalues being $> \lambda_{\rm th}$, while a filament point to two, a sheet point to one, and a void point to zero.

The classification of the cosmic web at a given point depends on the choice of $\lambda_{\rm th}$. It is still unclear which threshold value is the best. In Figure 4, we show the ratios of the volumes in the four types of structures to the whole volume (the volume filling fraction) as functions of $\lambda_{\rm th}$ at four different redshifts. Generally, the volume filling fractions for knots, filaments and sheets decrease with increasing $\lambda_{\rm th}$, while that for voids exhibits an opposite behavior. As discussed in Forero-Romero et al. (2009), the eigenvalues of the tidal tensor are not

only dynamical quantities, but also reflect the collapse timescale along the corresponding eigenvectors. Thus, these results reflect the collapse time distributions of the structures in three dimensions. Interestingly, the volume filling fraction defined with $\lambda_{\rm th} = 0$ show almost no variation with redshift. Theoretically, $\lambda_{\rm th} \sim 0$ corresponds to a very long collapse time, longer even than the Hubble time (Forero-Romero et al. 2009). It is thus not surprising that the fractions at $\lambda_{\rm th} = 0$ are independent of redshift. However, the dependence of the filling fraction on $\lambda_{\rm th}$ varies significantly with redshift: the change tends to occur in a narrower range of $\lambda_{\rm th}$ at higher redshift. By definition $\lambda_1 + \lambda_2 + \lambda_3 \equiv \delta_{\rm cs}$. Since the amplitude of the density fluctuation decreases with increasing redshift, the range of the three eigenvalues also decreases with increasing redshift, and so the behavior with $\lambda_{\rm th}$ is expected. The results for the reference simulation are presented for comparison. The fraction of filament (sheet) points in the constrained volume is slightly larger (smaller) than that in the whole box as well as in the reference simulation, likely because of cosmic variance. Overall, the average properties of the cosmic web in the CS are very similar to those of the reference simulation. More discussions about the cosmic web and its classification will be presented later (Section 5).

Embedded in these large structures are virialized dark matter halos formed through non-linear gravitational collapse. In the current paradigm of galaxy formation, halos are thought to be the hosts within which galaxies form and reside. They thus provide a key link between galaxies and the cosmic density field (e.g. Mo et al. 2010). Understanding the properties of the halo population, therefore, is an important step towards understanding galaxy formation. Furthermore, as demonstrated in Paper I, if the structure formation model employed in the HMC is not sufficiently accurate, it can induce non-Gaussian properties in the initial condition, which in turn can cause the predicted halo mass function to differ from what one expects to get from the model. Thus, investigating the properties of the halo population provides additional test of the reconstruction method. We select halos from each snapshot with the standard friend-of-friends (FoF) algorithm (Davis et al. 1985) with a link length equal to 0.2 times the average particle separation. The halo mass, $M_{\rm h}$, is the sum of the masses of all particles in the halo. Figure 5 shows the halo mass functions in both the whole box and the reconstruction volume at five different epochs. Our results excellently match the theoretical halo mass functions given by Sheth et al. (2001), except for the highest redshift where the theoretical model predicts higher number density of halos. This discrepancy at high-$z$ is very similar to the finding of Reed et al. (2003) in their (un-constrained) simulations, suggesting that it is due to the inaccuracy of the model at high $z$.

Halos grow hierarchically, with small halos forming first and merging to form large halos. After merger, the small halos may become substructures of the large one, producing a population usually called sub-halos. Host halos/subhalos and their merger histories extracted from $N$-body simulations have served as the backbone for semi-analytical model of galaxy formation (Kang et al. 2005; Croton et al. 2006; Guo et al. 2011; Lu et al. 2011) and other empirical models, such as subhalo abundance matching (Kravtsov et al. 2004; Vale & Ostriker 2006; Behroozi et al. 2010). To test the ability of our constrained simulation in reproducing the sub-halo population, we have identified sub-halos in all the FoF halos and constructed merger trees for all halos and sub-halos by using SUBFIND and other relevant codes kindly provided by Springel (Springel et al. 2005). In Figure 6, we show the sub-halo mass function for host halos in four mass ranges. Only sub-halos within the virial radii of their host halos and with more than 50 particles are counted. The mass functions have slopes very close to $-0.9$, in good agreement with results obtained previously (e.g. Gao et al. 2004; Diemand et al. 2004). The results for the reference simulation are also presented, both the amplitudes and shapes are in good agreement with the results from the CS. The full structure of a merger tree is complex and not easy to be presented in a simple way. Here we track the main branch (i.e. the most massive progenitor) of a $z = 0$ halo back in time until the time when the mass of the most massive progenitor is half of the final halo mass. The corresponding redshift, sometimes referred to as the formation redshift, is often used to represent the formation history of the halo. We show in Figure 7 the distributions of the formation redshift for

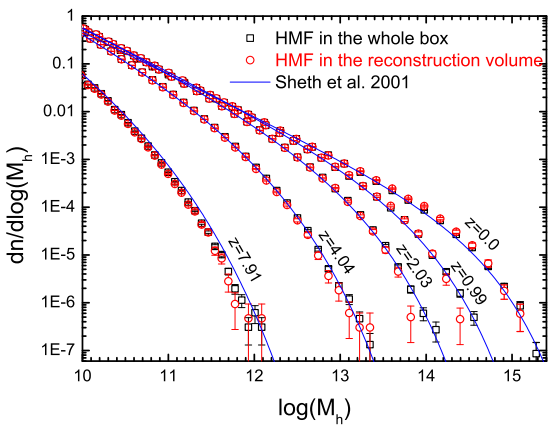


FIG. 5.— The halo mass functions at five different redshifts as indicated in the figures.

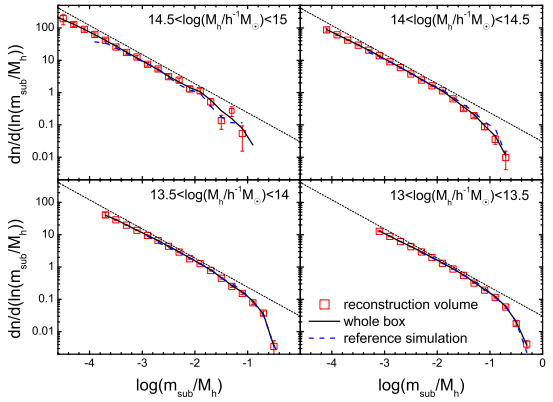


FIG. 6.— Sub-halo mass functions at redshift zero for four host halo mass ranges. The dotted lines show a slope of $-0.90$.

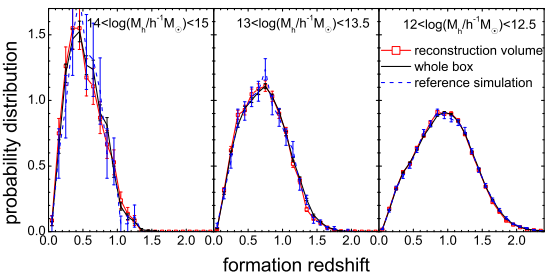


FIG. 7.— The probability distributions of the formation redshift of halos in three different mass ranges.

halo in three mass ranges. One can see that the distributions obtained from the CS match well those for reference simulation.

As a summary of this section, the statistical properties of our CS are very similar to those of general, unconstrained simulations, demonstrating that no significant bias is introduced by our reconstruction. With a resolution about 3 times as high as the widely-used Millennium Simulation (Springel et al. 2005), this simulation itself can be used to study many properties of the cosmic web (density, velocity and tidal fields, etc.), to construct mock catalogs of galaxies, to model galaxy-galaxy lensing, to study halo formation and distribution, and to generate halo merger trees to model galaxy formation. More importantly, our constrained simulation is unique in that it can be used to study directly the formation of the structures we observe, and the relation between the mass density field and real galaxies. Furthermore, it can also be used to set up zoom-in simulations in which the zoom-in region to be simulated with high resolutions needs to be designed so as to avoid contaminations by outside low-resolution particles during the evolution of the density field.

## 4. CORRELATIONS OF CONSTRAINED SIMULATION WITH REAL GROUPS AND GALAXIES

### 4.1. *Correlation between real groups and halos in the constrained simulation*

Since our reconstruction is based on the group catalog, it is expected that the CS density field to be tightly correlated with the spatial distribution of galaxy groups (Figure 1). Here we attempt to look for one-to-one correspondences between the groups and the FoF halos identified from the CS. Before doing this, let us first look at the spatial distributions of groups and halos. The left panel of Figure 8 shows the distributions of groups and halos with masses above $M_{\rm th} = 10^{12}\,h^{-1}{\rm M}_\odot$ in a $200 \times 200 \times 10\,h^{-1}$Mpc slice enclosing the Sloan great wall. On large scales, the spatial distribution of CS halos follows that of the groups very well. Inspecting individual groups, we can find that almost all of the massive groups (usually galaxy clusters) have corresponding FoF halos, However, their sizes and locations do not match perfectly. For systems of lower masses, the match becomes worse, but they still appear to reside in similar large scale structures.

To match groups and halos in a more quantitative way, we construct a galaxy group list and a halo list. The group list contains all groups with $M_{\rm gr} \geq M_{\rm th}$ in the reconstruction volume in decreasing order of group mass. Note that the redshift distortion for these groups has been corrected (Section 2.3). The halo list contains all FoF halos in the CS (with no limit on halo mass). For the first group (the most massive one) in the group list, we search in the halo list for halos with distances to the group less than $\Delta{\rm d}_{\rm mx}$ and with mass satisfying $|\log M_{\rm gr}/M_{\rm h}| \leq \Delta{\rm m}_{\rm mx}$. Here $M_{\rm gr}$ and $M_{\rm h}$ are group and halo masses, respectively. If no halo is found to satisfy the two criteria, the group is considered to have no match. Otherwise, we choose the halo with the smallest $|\log M_{\rm gr}/M_{\rm h}|$ as the corresponding halo of the group. Finally the group is removed from the group list, and the corresponding halo from the halo list. The procedure is repeated for all groups. This procedure assumes that large groups have more priority in match a halo than small groups, and mass matching has more priority than distance matching. The groups that have corresponding halos are referred to as matched groups, otherwise unmatched groups.

The number of matched pairs depends on the two free parameters, $\Delta{\rm d}_{\rm mx}$ and $\Delta{\rm m}_{\rm mx}$. In Figure 9, we show the fraction of matched groups as a function of both $\Delta{\rm d}_{\rm mx}$ and $\Delta{\rm m}_{\rm mx}$. Not surprisingly, as $\Delta{\rm d}_{\rm mx}$ and $\Delta{\rm m}_{\rm mx}$ increase, the number of matched groups increases. About half of the groups with $M_{\rm gr} \geq 10^{14}\,h^{-1}{\rm M}_\odot$ have matched halos with distances less than $1\,h^{-1}$Mpc and $|\log M_{\rm gr}/M_{\rm h}| < 0.15$. For $\Delta{\rm d}_{\rm mx} = 4\,h^{-1}$Mpc (the smoothing scale adopted in our HMC+PM) and $\Delta{\rm m}_{\rm mx} = 0.5$, then more than 95% of massive groups have halo matches. For comparison, we generate an uncorrelated halo sample by rotating the CS halos with a large angle. The matching results for the rotated halo sample are shown in red contours in Figure 9. One can see that the fraction of groups with matched halos is much smaller than 5% for the same two parameters.

For groups with masses $M_{\rm gr} \geq 10^{13}\,h^{-1}{\rm M}_\odot$, the matching becomes worse. For $\Delta{\rm d}_{\rm mx} = 4\,h^{-1}$Mpc, half of the groups have halo matches with $\Delta{\rm m}_{\rm mx} = 0.25$, and about 80% of the groups have halo matches with $\Delta{\rm m}_{\rm mx} = 0.5$. The corresponding fractions for the rotated halo sample are only 5% and 10%, respectively. For groups with $M_{\rm gr} \geq 10^{12}\,h^{-1}{\rm M}_\odot$, about 85% of groups are matched with CS halos with $\Delta{\rm d}_{\rm mx} = 4\,h^{-1}$Mpc and $\Delta{\rm m}_{\rm mx} = 0.5$. This does not mean that the matching is better for small halos, however, since for such a mass about 40% of the groups have matched halos in the rotated sample. Small halos are also much more abundant, so the probability for a group to be matched with an uncorrelated halo is larger.

For low mass groups, the match with CS halos is only slightly better than with uncorrelated halos. This suggests that the small scale modes in the initial condition are only partly recovered. However, as one can see from Figure 8, small groups and CS halos also trace the same large-scale structures. This indicates that the statistical properties of the small groups are strongly correlated with small halos in the CS. In order to quantify such correlations, we compare the correlation between the number density of small groups and that of CS halos on different scales. To this end, we divide the CS box into

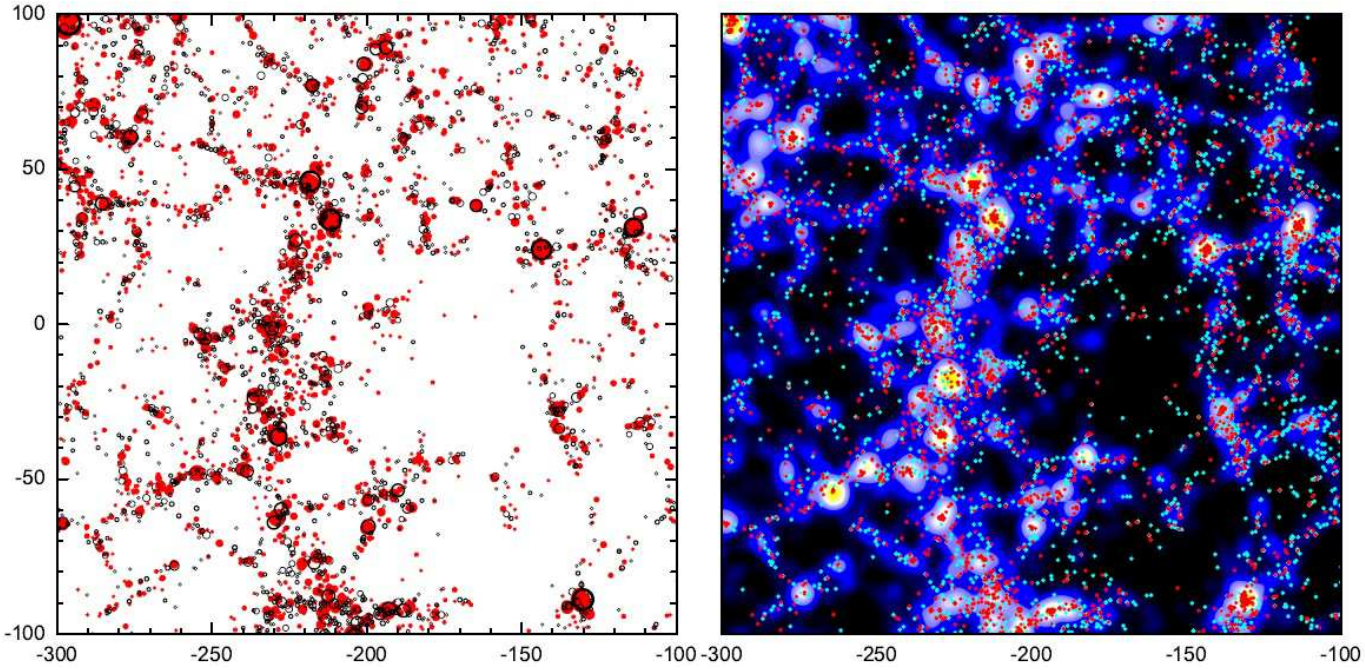


FIG. 8.— Left panel: the spatial distributions of SDSS galaxy groups (red solid circles) and dark halos in the CS (black open circles) in a $10\,h^{-1}$Mpc thick slice. Only groups and halos with masses larger than $10^{12}\,h^{-1}\mathrm{M}_{\odot}$ are shown. The symbol sizes of the groups and halos are proportional to their virial radii. Right panel: the mass density field together with the galaxy distribution in the same slice as in the left panel. The red (cyan) dots represent the red (blue) galaxies. The color code for the density field is the same as that in Figure 1.

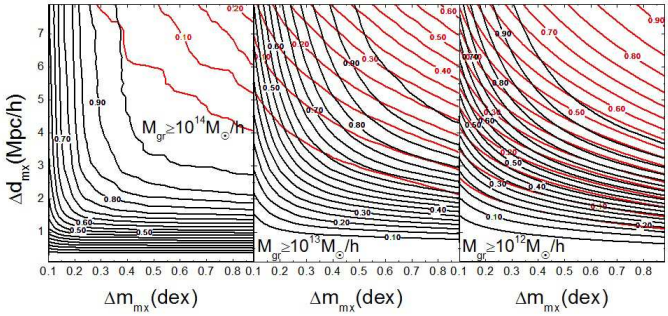


FIG. 9.— The black lines exhibit the cross-matching between galaxy groups and CS halos as a function of the maximum distance ($d_{\max}$) and maximum mass difference ($m_{\rm dex}$) for three group mass ranges. See the texts for details. The red lines show the results for uncorrelated halo sample, which is generated by rotating the CS halos with a large angle.

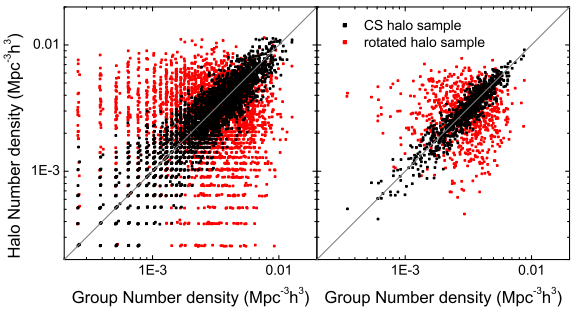


FIG. 10.— The number densities of CS halos (black dots) and rotated halos (red dots) versus the group number density estimated in cubes of $L_{\rm cb} = 20\,h^{-1}$Mpc (left panel) and $30\,h^{-1}$Mpc(right panel). Only halos and groups with masses between $10^{12}\,h^{-1}\mathrm{M}_{\odot}$ and $10^{13}\,h^{-1}\mathrm{M}_{\odot}$ are taken into account. The solid gray lines indicate the perfect relation.

cubes each with a size of $L_{\rm cb}$ on a side, and compute the number densities of groups, CS halos and halos in the rotated sample in each of the cubes. Figure 10 shows the density - density relation between groups and halos with masses in the range $10^{12}$ - $10^{13}\,h^{-1}\mathrm{M}_{\odot}$ for cubes with $L_{\rm cb} = 20\,h^{-1}$Mpc (left panel) and $30\,h^{-1}$Mpc (right panel), respectively. Here only cubes with at least 90% of their volumes are contained in the reconstruction volume are included. As one can see, the number densities of CS halos are tightly correlated with those of groups without any significant bias, and the correlation becomes tighter as $L_{\rm cb}$ increases. In contrast, no visible correlation can be seen between groups and halos in the rotated sample.

### 4.2. *Correlation between real galaxies and mass in the constrained simulation*

It is well known that galaxies are biased tracers of the cosmic density field (e.g. Peacock 1997; Jing et al. 1998). The bias is found to depend on both galaxy luminosity and color (Norberg et al. 2001; Zehavi et al. 2002; Li et al. 2006). Thus, the study of the correlation between galaxies and mass contains important information about galaxy formation. Almost all of the previous studies are concentrated on statistical measurements, such as (cross) correlation functions of galaxies. Here we present a one-to-one comparison between galaxy and mass densities sampled on a grid of cube.

To facilitate comparisons with the CS, we need to correct for the redshift distortions for galaxies. Our correction method consists of two steps. We first assign the

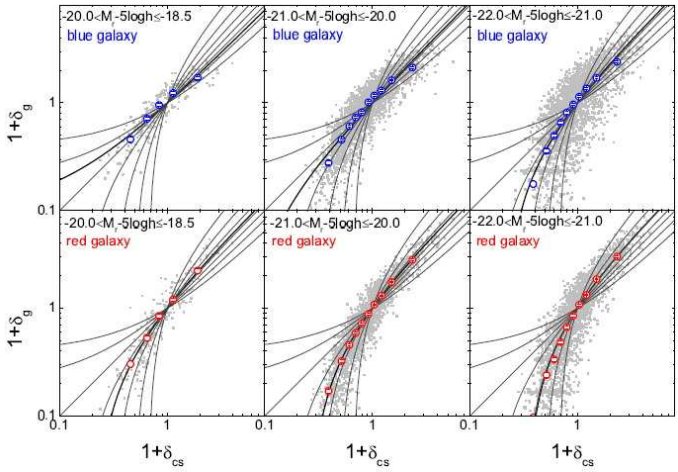


FIG. 11.— The correlations between galaxy densities and mass densities of the CS for galaxies of different magnitudes and colors, as indicated in the panels. $\delta_{\rm g}$ and $\delta_{\rm cs}$ are density contrasts for galaxies and mass, respectively. Each dot point represents the mean density in a cubic box with $L_{\rm cb} = 20\,h^{-1}$Mpc. The open circles with error bars are the mean values of the dot points. The thin lines show $\delta_{\rm g} = b\delta_{\rm cs}$, with $b = 0.6$, 0.8, 1.0, 1.2, 1.5, 2.0, and 3.0 (from left to right at $1+\delta_{\rm cs} < 1$), respectively. The thick lines are the best fits to the mean correlations.

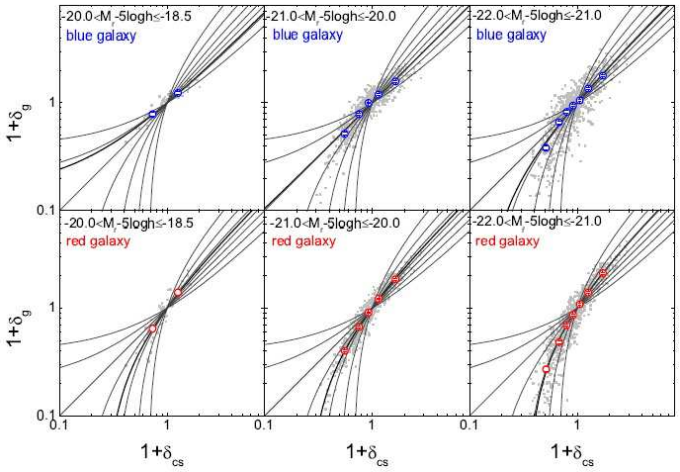


FIG. 12.— Similar to Figure 11 but here the densities are the averages in cubic boxes of $30\,h^{-1}$Mpc on a side.

group redshifts (after correction, see Section 2.2) to their member galaxies. Then for each satellite galaxy, we assign a random offset relative to its group center, along the line of sight, based on NFW profile (Navarro et al. 1997) with mass-concentration relation given by Zhao et al. (2009). The method can correct for both Kaiser effect and FOG effect, and make the spatial distribution of satellites within halos follow the NFW profile (see Shi et al. 2016 for more details). The right panel of Figure 8 shows the CS density field and galaxy spatial distribution. We separate red and blue galaxies according to their binormal distribution in the $g-r$ color - absolute magnitude plane (e.g. Baldry et al. 2004), using the same separation line as proposed by Yang et al. (2009):

$$g-r = 1.022-0.0651x-0.00311x^2, x = M_r-5\log h+23\,, \quad (4)$$

where $M_r - 5\log h$ are the absolute magnitude in the $r$ band. Note that both $M_{\rm r} - 5\log h$ and $g-r$ are $K-$corrected and evolution-corrected to redshift 0.1. The galaxy distribution match the CS density field very well. In addition, red galaxies appear more tightly associated with high density regions than blue ones.

To quantify the correlations in more detail, we select galaxies in three $M_r - 5\log h$ bins, $[-18.5,-20)$, $[-20,-21)$ and $[-21,-22)$, and separate each of them into red and blue subsamples. We estimate the galaxy density field for each galaxy subsample as follows. The galaxy subsample is embedded in the CS box and converted into a density field on a grid by using the clouds-in-cells (CIC) assignment (Hockney & Eastwood 1981). For a given subsample, we estimate the limiting redshift of completeness ($z_{\rm c}$) using equation (6) in Yang et al. (2009) and the corresponding co-moving distance $r(z_{\rm c})$. The intersection between the reconstruction volume and the sphere with radius $r(z_{\rm c})$ is referred to as the complete volume. Here, again, we divide the complete volume into equal-sized cubes. For each cube, the galaxy density contrast is defined to be $\delta_{\rm g} = \rho_{\rm g}/\bar{\rho}_{\rm g} - 1$, where $\rho_{\rm g}$ is the galaxy density in the cube and $\bar{\rho}_{\rm g}$ is the mean galaxy density in the complete volume. Using the same method, we also get the mass density contrast in each cube, $\delta_{\rm cs}$. In the following, we only consider the cubes that each have more than 90% of their volumes contained in the complete volume.

Figures 11 and 12 show $1+\delta_{\rm g}$ versus $1+\delta_{\rm cs}$ on two different scales, $L_{\rm cb} = 20$ and $30\,h^{-1}$Mpc, for the six galaxy subsamples defined above. Since the complete volume is different for different sub-samples, the number of cubes used varies. The galaxy density is strongly correlated with the CS mass density, and the scatter decreases with increasing $L_{\rm cb}$. Moreover, the galaxy density is biased with respect to the underlying mass density. To quantify this, we split each sample of cubes into several equal-sized subsamples according to $\delta_{\rm cs}$, and compute the mean $1+\delta_{\rm cs}$ and $1+\delta_{\rm g}$ for each subsample. The mean correlations are shown as open circles in the figures. The galaxy bias is usually interpreted in terms of halo bias (e.g. Mo et al. 1996). We thus use the bias relation $\delta_{\rm g} = b\delta_{\rm cs}$ to fit the mean results, and show the best-fitting models in thick lines in the figure. The corresponding bias parameters are list in Table 1. The relations with $b = 0.6$, 0.8, 1.0, 1.2, 1.5, 2.0, and 3.0 are also plotted as references.

In general, the mean correlations can be well fitted by the theoretical model, and the bias factor tends to be larger for higher luminosity and for red galaxies. In particular, the bias factors obtained here match well those obtained by Zehavi et al. (2011), who measured the bias as the square root of the ratio of the two-point correlation functions between galaxies and dark matter assuming a fiducial cosmological model. Inspecting closely the fitting curves, we find that the single-bias model fit the observational data better for red galaxies than for blue galaxies. Moreover, for a given luminosity, the correlation also appears tighter for red galaxies. One possible explanation for these results is that, for a given luminosity, blue galaxies tend to reside in halos with a wider range of halo masses than red galaxies. In a future paper, we will investigate the correlation between the galaxy population and the reconstructed density and tidal fields in detail.

## 5. COSMIC WEB IN THE SDSS VOLUME

TABLE 1
GALAXY BIAS FOR VARIOUS GALAXY SUBSAMPLES

| | | | |
|---|---|---|---|
| | $L_{\rm cb} = 20\,h^{-1}$Mpc | | |
| $M_{\rm r}$ bin | $[-18.5,-20)$ | $[-20,-21)$ | $[-21,-22)$ |
| blue | $0.90 \pm 0.03$ | $1.08 \pm 0.01$ | $1.29 \pm 0.01$ |
| red | $1.29 \pm 0.04$ | $1.37 \pm 0.01$ | $1.52 \pm 0.01$ |
| | $L_{\rm cb} = 30\,h^{-1}$Mpc | | |
| blue | $0.84 \pm 0.08$ | $0.99 \pm 0.02$ | $1.16 \pm 0.03$ |
| red | $1.37 \pm 0.15$ | $1.35 \pm 0.02$ | $1.53 \pm 0.02$ |

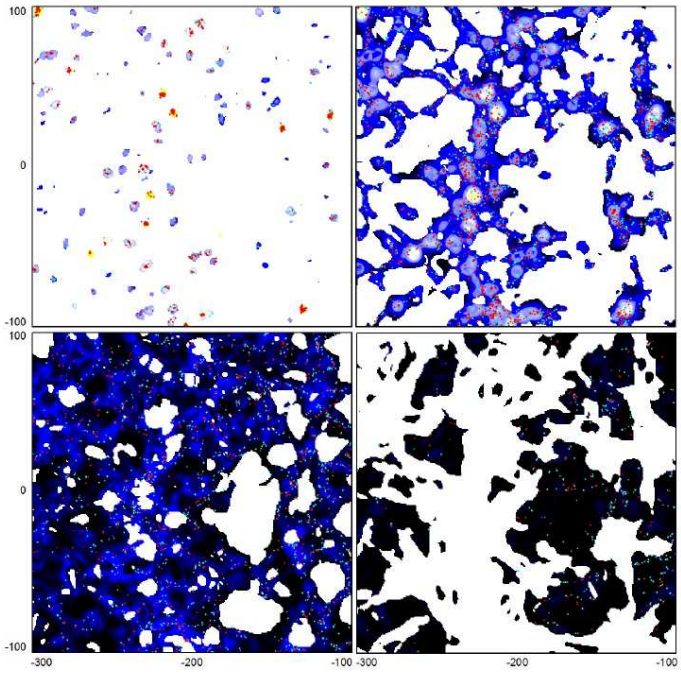

FIG. 13.— The projected density fields and galaxies in volumes classified as knots (top left), filaments(top right), sheets (bottom left) and voids (bottom right). The red and cyan points represent red and blue galaxies respectively. The color code for the density field and the slices are the same as those in Figure 8.

One of the most prominent structures in our local Universe is the Sloan Great Wall which is at $z \sim 0.08$. Figure 8 shows part of this massive structure, which contains several galaxy clusters. A large, low-density region containing only a few galaxies lies on the right side of the Great Wall. Galaxy formation efficiency appears to be very different in the two different regions. In order to understand this, it is useful to classify the large scale structures into different categories to represent their dynamical properties. As discussed in Section 3, local tidal tensor may provide a useful way to classify the cosmic web. Here we show the classification using $R_{\rm s} = 2\,h^{-1}$Mpc and $\lambda_{\rm th} = 0.2$ (see e.g. Forero-Romero et al. 2009). The projected density maps for the four different web types, knots, filaments, sheets and voids, are separately shown in the four panels of Figure 13. The slice is the same as that shown in Figure 8, i.e. of $10\,h^{-1}$Mpc thick. At any position on the projected 2-dimensional map, there are 10 grid cells projected along the direction perpendicular to the slice. Since it is likely that the 10 overlapping grids belong to different categories, there are overlaps between different web types. If no grid cell at a given position in the slice is classified as the web type in question, the position at the corresponding panel is plotted in white color. One can see that the Sloan great wall is identified as a filamentary structure, percolating the whole slice in the vertical direction, while the low density region is classified as a void. Cells classified as sheet occupy a very large part of the plot, although the volume of the sheet cells is only about 40% of the total. This implies that the sheet structures are thin. Galaxies are also separated into four types, based on the locations of their host groups, and their positions are superposed on the corresponding projected density fields. The knot galaxies have the highest galaxy density and the FOG effect has been corrected by our method. The distribution of filament galaxies is more concentrated than those of sheet and void galaxies. Inspecting the two low-density environments (sheets and voids), we see that galaxies tend to reside in relatively high density regions. In particular, red galaxies are more abundant than blue ones in knots but less abundant in voids, in broad agreement with previous results based on galaxy clustering (e.g. Li et al. 2006).

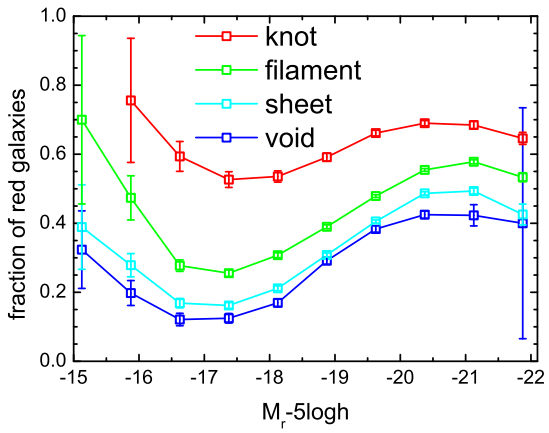


FIG. 14.— The fractions of red galaxies as functions of the $r$-band absolute magnitude. The color-coded lines show the results for galaxies residing in knots, filaments, sheets and voids as indicated.

To investigate the environmental dependence of galaxy color quantitatively, we show in Figure 14 the fraction of red galaxies in the four environments as a function of the $r$-band magnitude. For all the luminosity bins, the red fraction is the highest for knot galaxies, followed successively by filament, sheet and void. For knot galaxies, the fraction is slightly more than 60% on average and exhibit a weak dependence on galaxy luminosity if the data point at the lowest luminosity, which has a large error bar, is excluded. For filament, sheet and void galaxies, the fraction varies with luminosity in a non-monotonous way, in the sense that it first decreases then increases as the luminosity increases. These results reflect the complicated quenching processes, such as environmental quenching and mass quenching (e.g. Peng et al. 2010). Since we know that the halo population is different in different structures (see Hahn et al. 2007), one interesting question is whether these environmental processes can be explained in terms of the differences in the halo population. Studying this problem may help us to understand the role of large scale structure in galaxy formation. In a future work, we will use the CS and group catalog to investigate

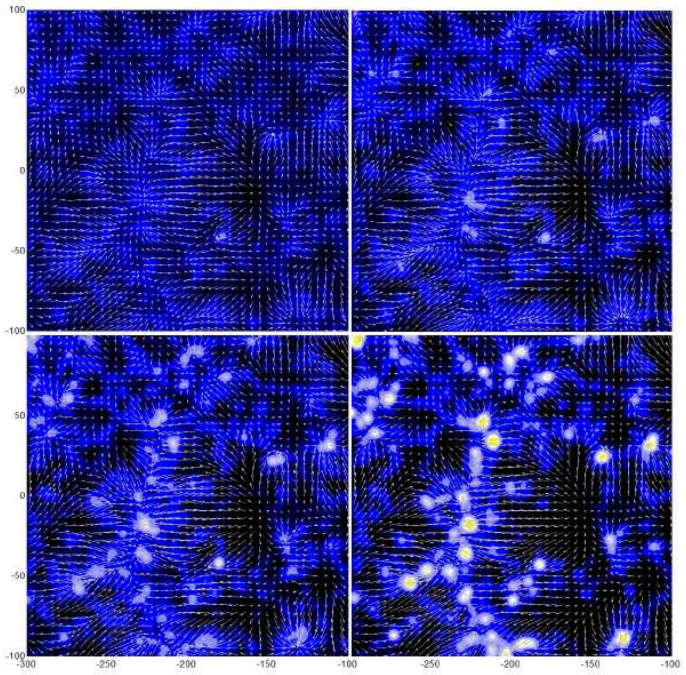

FIG. 15.— The evolution of the density (color maps) and velocity (arrows) fields in a slice of $10\,h^{-1}$Mpc thick enclosing part of the Sloan Great Wall. The four panels show the results at $z = 4.04$ (top-left), $z = 2.03$(top-right), $z = 0.99$ (bottom-left) and $z = 0$ (bottom-right), respectively. The color coding is the same as that in Figure 1. The length of a arrow is proportional to the magnitude of the velocity it represents.

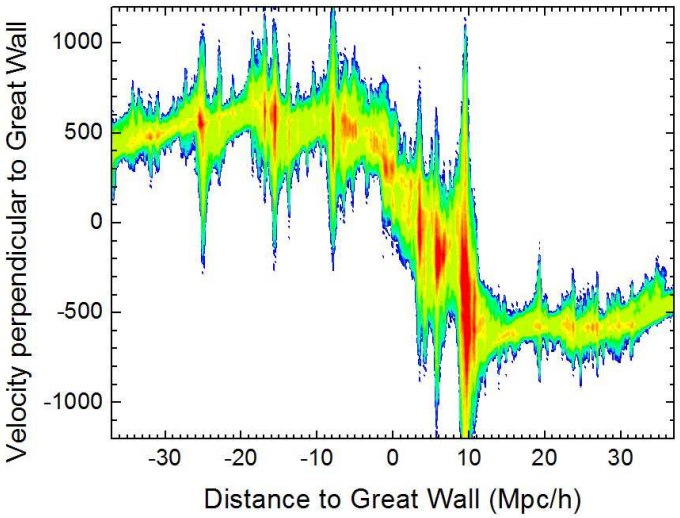


FIG. 16.— The phase-space distribution for dark matter particles within a column. The symmetric axis of the column is perpendicular to the Sloan great wall and its radius is $5\,h^{-1}$Mpc. The velocities and distances shown are all projected onto the symmetric axis of the column. Distance equal to zero indicates the great wall location. Red color denotes high phase-space density while blue denotes low phase-space density. White regions are empty of particles.

this question further.

One advantage of the constrained simulation is that it can reveal the dynamical state and formation history of the large scale structures. In Figure 15 we show the density fields together with the velocity fields around the Sloan great wall at four different redshifts. If searching for the Sloan great wall only through the density contrast, one cannot see any sign for the great wall before $z \simeq 4$, but it starts to show sign at $z \simeq 2$. By $z \simeq 1$ the great wall grows into a dominant structure in the slice. Since then it becomes more concentrated but its co-moving length changes only little. Its strong gravity empties the nearby region, forming a big void at the right. On the other hand, the evidence for the existence of the wall can be seen in the velocity field at $z \simeq 4$. The velocity field clearly reveals that the great wall continues to attract material from the left and right sides during almost the entire history of the Universe. Compared to the perpendicular component, the velocity component along the filament is very small, so that the collapse along this direction is prolonged. This is consistent with the theoretical expectation for the mass flows around filamentary structures, and such flow pattern can affect the dynamical properties of the halos residing in filaments (Shi et al. 2015).

To show the accretion flow around the Sloan great wall in more details, we define a column that is perpendicular to the filament and show the phase-space distribution for dark matter particles within this column in Figure 16. To avoid the contamination of particles in massive clusters, we place the center of the column between two massive clusters, which are separated by about $19\,h^{-1}$Mpc. The radius and length of the column are set to be $5\,h^{-1}$Mpc and $80\,h^{-1}$Mpc, respectively. The velocity and distance (to the center of the column) are both projected onto the rotation axis of the column. One can clearly see that the materials in the column flow towards the filament from both the near and far sides. In the outer region where the distance to the great wall is larger than about $5\ h^{-1}$Mpc, the mean velocity remains more or less at a constant level, around $500\,\mathrm{km\,s^{-1}}$. Since the great wall is quite straight (Figure 1) and much longer than the scale considered here, its gravity over this scale depends only weakly on the distance to it. In the linear regime, the velocity is proportional to the gravity, and so the constant velocity may be explained by the straight filamentary structure. In the inner region, on the other hand, the flow velocity decreases with decreasing distance, indicating that the width of the great way is less than $10\,h^{-1}$Mpc. The velocity dispersion in the inner region appears larger than that in the outer region – note again that the column is not centered on any cluster, which is likely caused by the collision of the convergent flow. Such collisions are expected to heat the associated inter-galactic medium to high temperatures, which may be observed through UV absorption, X-ray emission, and Sunyaev-Zel'dovich effect. Moreover, the heating might also quench gas accretion into small halos embedded in the filaments, eventually affecting galaxy evolution in such environments (Mo et al. 2005). The Sloan Great Wall is therefore a wonderful place for studying the inter-galactic medium and the interaction between galaxies and the large-scale structure. Constrained hydrodynamical simulations are needed in order to address this problem in detail.

Another interesting object in the nearby Universe is the Coma galaxy cluster. The simulated halo corresponding to this cluster has almost the same mass and position: the Coma galaxy cluster has an estimated mass of $9.1 \times 10^{14}\,h^{-1}\mathrm{M}_{\odot}$ in Yang et al (2007) catalog, and

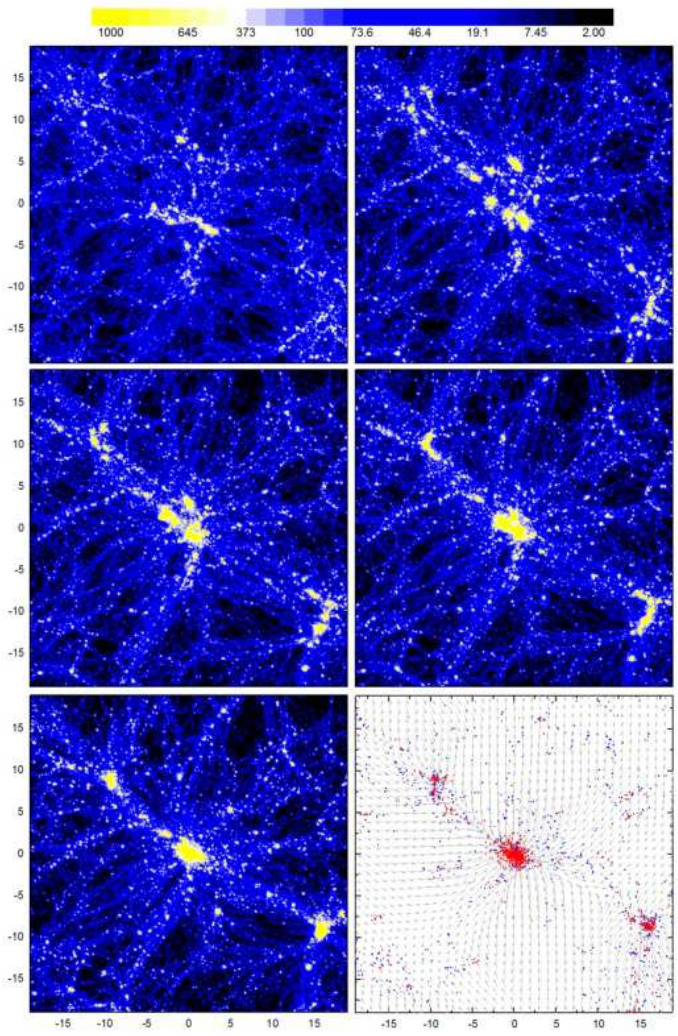


FIG. 17.— The projected mass density fields in a slice of $39 \times 39 \times 10\,h^{-1}$Mpc centered on the Coma cluster at $z \sim 2$ (top-left), $z \sim 1$ (top-right), $z \sim 0.5$ (middle-left), $z \sim 0.3$ (middle-right) and $z = 0$(bottom-left). The bottom-right panel shows the spatial distribution of real galaxies and the velocity field extracted from the CS.

the corresponding halo is only 0.04 dex larger, about $1.0 \times 10^{15}\,h^{-1}\mathrm{M}_{\odot}$; the spatial separation between the real cluster and the simulated halo is only $0.018\,h^{-1}$Mpc. In addition, they also have similar shapes in projection. Figure 17 shows the projected CS density map and galaxy distribution in a slice of $39 \times 39 \times 10\,h^{-1}$Mpc centered on the Coma cluster. The projected direction is chosen to be parallel with the line of sight to the Coma cluster. One can see that the galaxy distribution within the Coma cluster aligns with the mass distribution of the halo. It is known that massive halos are strongly aligned with the large scale structures within which they are embedded (e.g. Hahn et al. 2007; Wang et al. 2011). Since our method can reliably recover the large scale structures, it is not surprising to find the similar alignments between the observed galaxy distribution and the CS mass distribution. Nevertheless, it suggests that the CS can be used to study various alignments between galaxies/galaxy systems with the large scale structures (e.g. Brown et al. 2002; Faltenbacher et al. 2009; Zhang et al. 2013).

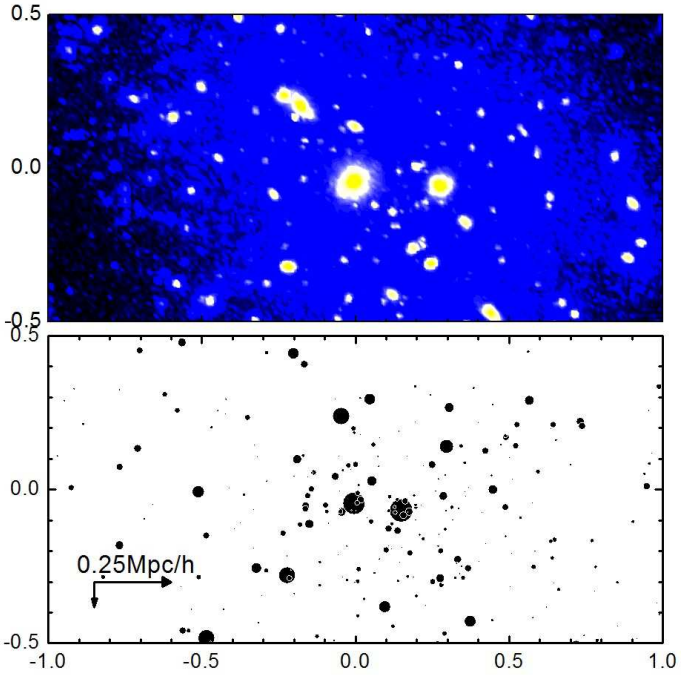


FIG. 18.— The upper panel shows the inner region of the Coma cluster in the CS. Different from other density maps, this figure is color-coded by the square of the projected densities so that the substructures can be seen more clearly. In lower panel, the black dots show the spatial distributions of real galaxies in the Coma galaxy cluster. The symbol sizes are scaled with the galaxy luminosities, and all galaxies are shifted horizontally by $\sim 0.25\,h^{-1}$Mpc and vertically by $\sim 0.08\,h^{-1}$Mpc (as indicated by the arrows).

Figure 17 illustrates again how our method can reliably recover the large scale structures. For instance, in addition to the Coma cluster, the other two massive groups, located respectively in the bottom-right and top-left corners, also have corresponding massive halos. The massive filament connecting the three galaxy systems and the surrounding big voids are also reproduced by the CS. The velocity field obtained from the CS is superposed on the galaxy distribution in the bottom-right panel. The flows converge to the three massive galaxy groups/clusters. A filamentary flow pattern towards the Coma cluster is also clearly seen, which corresponds to the massive filament in the density map. Recall that the flow along the Sloan great wall is quite slow, which is very different from what we are seeing here.

The CS reveals the possible formation history of the Coma cluster and the nearby structure (Figure 17). At $z \simeq 2$, only several compact and thin filamentary structures embedded in an over-density region are produced. These filaments collapse and merge to form a number of halos at $z \sim 1$. These halos then move close to each other and merge to form two massive halos of comparable sizes surrounded by numerous small halos. Meanwhile, thin filaments, which appear parallel, are assembling into thick filaments connected to the Coma cluster observed at $z = 0$. The velocity field reveals that the Coma cluster is still accreting material through the filaments even at the present day. The CS suggests that the Coma cluster has experienced a violent merger in the recent past ($z \sim 0.3$). The upper panel of Figure 18 shows the zoom-in of the dark matter halo of the

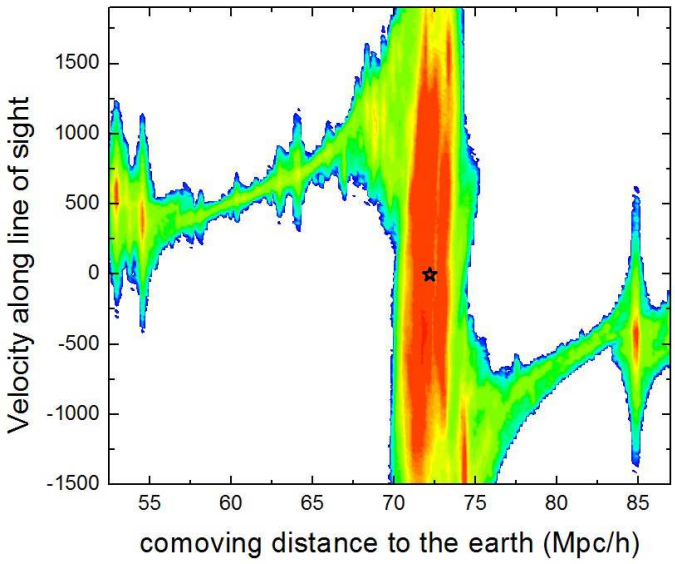


FIG. 19.— The phase-space distribution for dark matter particles within a column. The symmetric axis of the column is the line of sight to the Coma cluster and its radius is $2.5\,h^{-1}$Mpc. The velocities and positions shown are projected onto the line of sight. The star indicates the velocity and position of the Coma cluster. Red color denotes high phase-space density while blue denotes low phase-space density. White regions are free of particles.

Coma cluster at $z = 0$. Two high density peaks in the (projected) central region, which are the vestiges of the major merger, are clearly seen. It is interesting to compare these results with the observational properties of the Coma cluster. In the lower panel of Figure 18, we show the galaxy distribution in the central region of the Coma cluster with a slight ($\sim 0.25\,h^{-1}$Mpc) offset. The spatial distribution of luminous galaxies resembles that of the massive substructures. In particular, the two supergiant elliptical galaxies in the central region (see also Fitchett & Webster 1987) roughly match the two high density peaks, and may indeed correspond to the central galaxies that formed earlier in the two massive progenitors seen at $z > 0.3$. Observations at other wave bands also support this merger scenario for Coma. For example, X-ray observations suggested that the Coma cluster is unrelaxed (e.g. Briel et al. 1992; Sanders et al. 2013); radio observations revealed the presence of a radio relic (Giovannini et al. 1985), which might be produced by shock waves (Enßlin et al. 1998; Miniati et l. 2001) produced by the merger of the two massive progenitors. These results clearly demonstrate the power of our reconstruction in understanding the histories and structures of massive objects observed in the nearby Universe. A movie, showing the 3-dimensional structure of the simulated Coma cluster and the comparisons with optical and X-ray observations, is shown at http://staff.ustc.edu.cn/~whywang/MOVIE/.

Finally, in Figure 19, we show the phase-space distribution of dark matter particles within a column, with its axis along the line of sight (LOS) to the Coma cluster and a radius of $2.5\,h^{-1}$Mpc, comparable to the virial size of the Coma cluster. The velocity and position are both projected onto the LOS, with the cluster center denoted by a star. Due to the gravitational attraction of the cluster, the bulk velocity of the surrounding material increases with decreasing distance to the cluster, reaches as high as $1000\,\mathrm{km\,s^{-1}}$ on average. At locations far from the cluster, dark matter particles occupy a very narrow range in velocity, indicating that the velocity dispersion of the structure is quite low. However, as the distance to the Coma decreases to about $5\,h^{-1}$Mpc (about 2 times of the virial radius), the velocity dispersion starts to increase with decreasing distance, and the increase becomes very rapid as the distance approaches $\sim 2\,h^{-1}$Mpc. Within $2\,h^{-1}$Mpc, the phase-space distribution are dominated by random motion within the cluster while the bulk motion becomes negligible (see the black star). The sharp edge indicates that the cluster size is about $2\,h^{-1}$Mpc. The presence of substructures within $2\,h^{-1}$Mpc can be seen clearly, consistent with the results shown above.

The examples described above demonstrate clearly that the constrained simulations can provide much environmental and dynamical information for the observed galaxies and galaxy systems. To check the reliability of such environmental and dynamical information, we have made tests using mock catalogs and estimate the uncertainties of the predicted tidal and velocity fields. The results are presented in the appendix. To summarize, the uncertainties in the three eigenvalues of the tidal tensor estimated from the CS density field are similar, about 0.2 for a smoothing radius $R_{\rm s} = 4\,h^{-1}$Mpc, and increasing to $\sim 0.6$ at $R_{\rm s} = 2\,h^{-1}$Mpc. The uncertainty in the velocity field depends on the distance to the boundary of the reconstruction volume, because the structures outside the reconstruction volume are not constrained. We divide the reconstruction volume into three parts, the inner, intermediate and boarder regions, according to their "distances" to the boundary. The uncertainties of the one dimensional velocity in the three regions are about 80, 132 and $195\,\mathrm{km\,s^{-1}}$, respectively, at the smoothing radius of $4\,h^{-1}$Mpc. As the smoothing scale decreases to $2\,h^{-1}$Mpc, the uncertainties remain more or less the same. This is expected because gravitationally generated velocities are dominated by large scale modes of the cosmic density field.

## 6. SUMMARY

In our previous studies (Yang et al. 2005;2007; Wang et al. 2009;2012;2013; Paper I) we have developed a series of methods to reconstruct the initial density field from a galaxy redshift survey. These methods have been tested in great detail with $N$-body simulations and mock galaxy catalogs. In this paper, we apply these methods to the SDSS DR7 galaxy sample at $z \leq 0.12$. We start with galaxy groups identified from this sample by the halo-based group finder of Yang et al. (2005, 2007) and use them to represent dark matter halo population. Redshift distortions in the distances of the groups are corrected by using the peculiar velocities of the groups predicted by the reconstructed density field. We then adopt the halo-domain method of Wang et al. (2009) to reconstruct the present-day density field from the distribution of the halo population in real space. The initial density field for the formation of the local universe is reconstructed from the present-day density field by using the Hamiltonian Markov Chain Monte Carlo algorithm combined with the PM dynamics that evolves the initial density field to the density field today (Paper I). And finally, the reconstructed initial density field is used as

the initial condition for an $N$-body simulation to obtain a constrained simulation (CS). This CS assumes WMAP5 cosmology and trace the evolution of $3072^3$ particles in a periodic cubic box of $500\,h^{-1}$Mpc on a side. Tests with mock galaxy catalog indicate that the reconstruction is reliable, with an uncertainty in the mass density of about 0.10 (0.23) dex, in the tidal field of about 0.2 (0.6), in the velocity field of $\leq 130\,\mathrm{km\,s^{-1}}$ ($\leq 136\,\mathrm{km\,s^{-1}}$) on a scale of $4\,h^{-1}$Mpc ($2\,h^{-1}$Mpc) at $z = 0$. Our investigations show that the main sources of the uncertainties in the reconstruction are the redshift distortion and the inaccuracy of the group finder.

We present results for a number of important statistics of the constrained simulation on various scales, such as the mass power spectra, the volume fractions of different types of the cosmic web, the halo mass function, and their evolutions with time. We also identify sub-halos and construct merger trees for both halos and sub-halos. The results are in good agreement with theoretical predictions and with those given by a reference simulation that assumes random initial phases. All these demonstrate that our reconstruction is unbiased.

We then investigate the relation of the CS with real groups and galaxies. We cross match the observed groups with the FOF halos identified from the CS. About half of the SDSS groups with masses larger than $10^{14}\,h^{-1}\mathrm{M}_\odot$ have matched halos with distances less than $1\,h^{-1}$Mpc and mass differences less than 0.15 dex. Choosing the maximum distance difference to be $4\,h^{-1}$Mpc and the maximum mass difference to be 0.5 dex results in 95% and 80% of the groups with $M_{\rm gr} \geq 10^{14}\,h^{-1}\mathrm{M}_\odot$ and $\geq 10^{13}\,h^{-1}\mathrm{M}_\odot$ having matched halo. The matched fractions are much higher than those between the groups and halos in a rotated sample, which are <5% and 10% for the above two cases, respectively. For smaller groups ($\geq 10^{12}\,h^{-1}\mathrm{M}_\odot$), the matched fraction is 85%, slightly larger than that between the groups and rotated halo sample, which is 40%. Thus, the one-to-one match is robust for cluster-sized halos but marginally so for galactic-sized halos. However, the number density of groups with $10^{12}\,h^{-1}\mathrm{M}_\odot \leq M_{\rm gr} \leq 10^{13}\,h^{-1}\mathrm{M}_\odot$ in small cubes ($20\,h^{-1}$Mpc on a side) is tightly correlated with that of CS halos in the same mass range, much tighter than that between random pairs of cubes. This suggests that the statistics for small groups are also well reproduced in volumes much smaller than the reconstruction volume, and so cosmic variance is effectively reduced in the constrained simulation. The reliability of the matching depends directly on the accuracy of the PM model used in the HMC. One can, therefore, improve the reconstruction by adopting PM models of higher accuracy. The good match between massive groups and CS halos suggests that one can rely on the CS to study the histories of individual galaxy systems, at least for massive ones. We use the Coma cluster and the SDSS great way as examples to demonstrate how the CS can be used to study the formation history, density and velocity field in and around known observed structures.

We also investigate the correlations between the mass density obtained from the CS and galaxies in the reconstruction volume. Strong correlations are found, and bias in the distribution of galaxies with respect to the mass is clearly seen, being stronger for high-luminosity and red galaxies. The correlation with the mass density field is found to be tighter for red galaxies than for blue galaxies of the same luminosity, indicating that red galaxies are better in tracing the mass density. This connection between the observed galaxies and the underlying mass density provides a direct way to investigate how the bias depends on galaxy properties and how the scatter between the two density fields is produced. We will come back to a detailed investigation on this in a future paper. Based on the CS density field, we classify the cosmic web in the SDSS volume into four categories, knot, filament, sheet and void, based on the local tidal tensors obtained from the CS. We find that the fraction of red galaxies is the largest in knots, followed by filaments, sheets and voids, for almost all luminosity ranges considered.

The constrained simulation presented in this paper have many other applications in the future. For instance, we can model galaxy formation using halos and merger trees extracted from the CS combined with the galaxy formation models, such as the semi-analytic model and other halo-based empirical models. The modeled galaxies will guaranteed to have similar spatial distribution to the real galaxies, and environmental effects in halo formation will be automatically taken into account. This will make the comparison between models and observations statistically more robust and free of cosmic variance. Furthermore, we can carry out gas simulations directly from the reconstructed initial condition to study the interactions between galaxies, gas, and dark matter in different regions of the observed universe. Such an approach is particularly useful in probing the gas components and its evolution in massive large scale structures and massive galaxy clusters, for which there are one-to-one correspondences between the observation and the CS. For example, the converging mass flow towards the Sloan great wall has quite high velocities. The gas simulation can help us to understand the state of the gas associated with the great wall, and to examine the influence of such a large structure on the cooling and condensation of gas in dark matter halos embedded in the structure. The constrained simulations can also provide information about the large-scale environments and their dynamical states for galaxies and galaxy systems. An analysis of the correlation between galaxy intrinsic and environmental properties can then be made straightforwardly, which can provide constraints on how galaxies form and evolve in the cosmic density field.

## ACKNOWLEDGMENTS

This work is supported by the 973 Program (2015CB857002,2015CB857005), NSFC (11522324,11421303,11233005,11533006,11320101002), the Strategic Priority Research Program "The Emergence of Cosmological Structures" of the Chinese Academy of Sciences, Grant No. XDB09010400 and the Fundamental Research Funds for the Central Universities. H.J.M. would like to acknowledge the support of NSF AST-1517528. The work is also supported by the Supercomputing Center of University of Science and Technology of China and the Center for High Performance Computing, Shanghai Jiao Tong University.

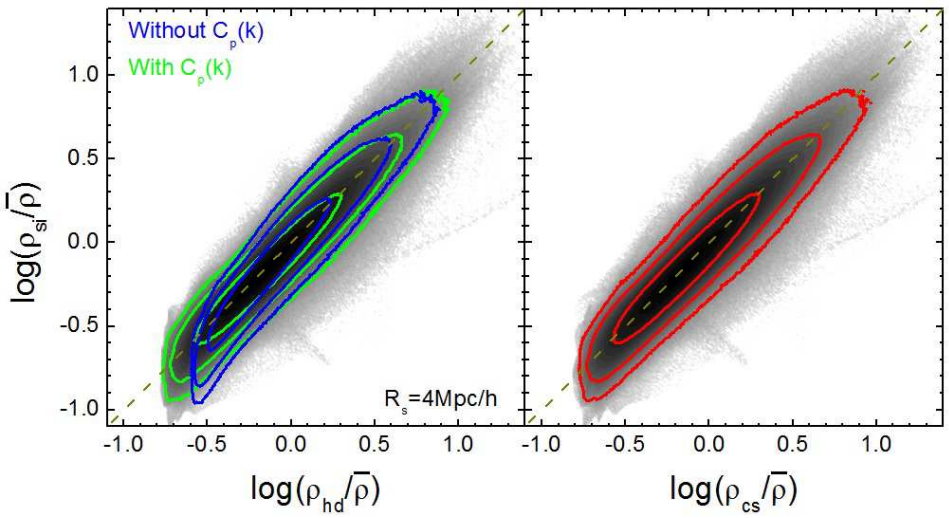


FIG. 20.— Density-density plots between the original MS simulation($\rho_{\rm si}$) and the halo-domain reconstruction ($\rho_{\rm hd}$, left panel), and between the MS and the CS ($\rho_{\rm cs}$, right panel). The density fields are smoothed with a Gaussian of radius $R_{\rm s} = 4\,h^{-1}$Mpc. The three contours encompass 67%, 95%, and 99% of the grid cells in the reconstruction volume. The dashed lines indicate the perfect relation. In the left panel we also include the results for the halo-domain reconstruction that does not include the correcting function ($C_{\rm p}(k)$) for comparison (blue contour). Please see Appendix for details.

## APPENDIX

## TESTS WITH MOCK CATALOG

To estimate the uncertainties of our reconstruction, we use a mock galaxy catalog to test our methods described in Section 2. The mock galaxy catalog is exactly the same as that used in Wang et al. (2012; 2013) and constructed in a way similar to that described in Yang et al. (2007). The mock galaxy catalog is built from the 'Millennium Simulation' (MS) carried out by the Virgo Consortium (Springel et al. 2005). We populate galaxies in dark matter halos identified from the MS according to the conditional luminosity function model (CLF) of van den Bosch et al. (2007) and assign phase-space coordinates (positions and peculiar velocities) to these galaxies following Yang et al. (2004). Note that the peculiar velocities of galaxies include the contribution of both the motions of the host halos and virial (random) motion of galaxies within their host halos. We then stack $3\times3\times3$ galaxy-populated simulation boxes together and place a virtual observer at the center of the stack. With respect to the observer, each galaxy is assigned ($\alpha_{\rm J}$, $\delta_{\rm J}$) coordinates and a redshift, which is a combination of its cosmological redshift and peculiar velocity. Finally, a mock galaxy catalog is constructed by mimicking the sky coverage of the SDSS DR7, taking into account the angular variation of the magnitude limit and survey completeness (see Li et al. 2007). Readers are referred to Wang et al. (2012; 2013) for details.

We apply the halo-based group finder of Yang et al. (2005; 2007) to the mock galaxy catalog and obtain a mock catalog of groups, with masses assigned according to the characteristic luminosities of individual groups (Section 2.1). Redshift distortions are corrected for the mocked groups and the halo-domain method is used to reconstruct the present-day density field ($\rho_{\rm hd}$), following exactly the same methods described in Section 2.2 and 2.3. We then reconstruct the initial density field from $\rho_{\rm hd}$, using the HMC+PM method with the same spatial and time resolutions as those described in Section 2.4. Finally, the reconstructed initial density field is evolved to the present day with Gadget-2. Thus, all procedures used here for the mock catalog are exactly the same as that given in Section 2 for the SDSS catalog. The only main difference is that here we use the same cosmology as adopted in MS, which is different from WMAP5 adopted in this paper, and a lower mass resolution for the constrained simulation ($800^3$ particles).

The density-density relation between $\rho_{\rm hd}$ and the original density field $\rho_{\rm si}$, both smoothed with $R_{\rm s} = 4\,h^{-1}$Mpc, is shown in the left panel of Figure 20. One sees that $\rho_{\rm hd}$ follows $\rho_{\rm si}$ without significant bias. The typical scatter, in terms of the r.m.s of $\log(\rho_{\rm si}/\rho_{\rm hd})$, is about 0.09 dex. For a smaller smoothing radius, $R_{\rm s} = 2\,h^{-1}$Mpc, the scatter increases to 0.20 dex. For comparison, we also show the density field from the halo-domain reconstruction without applying any correction to the Fourier modes (see Section 2.3 for details). As one can see, the correction function lowers the density at the lowest density end of $\rho_{\rm hd}$ while having little effects at in high density regions, making $\rho_{\rm hd}$ better in matching the original density field, $\rho_{\rm si}$. The right panel of Figure 20 presents the comparison between the density fields of the constrained simulation (CS) and the original simulation. The correlation is very similar to that between $\rho_{\rm hd}$ and $\rho_{\rm si}$. This is expected as the correlation between $\rho_{\rm hd}$ and $\rho_{\rm cs}$ is very tight, with scatter of only 0.02 dex. Overall, the CS density field matches the original one very well; the typical scatter between the two is 0.10 dex at $R_{\rm s} = 4\,h^{-1}$Mpc and 0.23 dex at $R_{\rm s} = 2\,h^{-1}$Mpc. These tests demonstrate that our HMC+PM method is accurate; the main errors are produced by the reconstruction of the current density field, i.e. from the uncertainties in redshift distortion correction, in the group finder, and in the density model based on halo domains.

Next we consider the cosmic tidal field, which provides important environmental information for studying galaxies and dynamical information to study the large-scale structure. Figure 21 shows the three eigenvalues of the tidal tensor

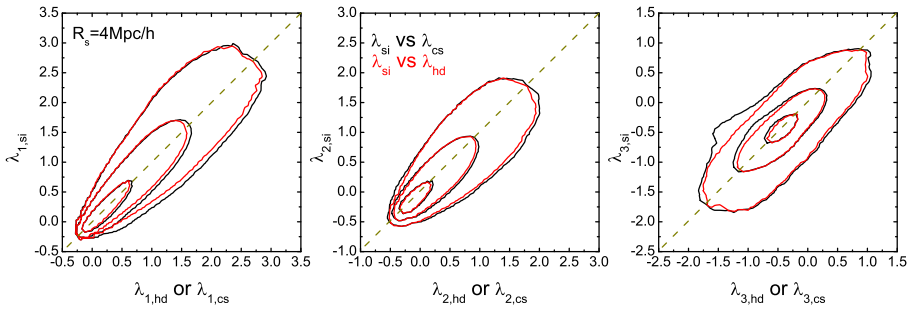


FIG. 21.— The three eigenvalues of the tidal tensor obtained from the original simulation ($\lambda_{\rm si}$) versus those obtained from the halo-domain reconstruction ($\lambda_{\rm hd}$, red) and the CS ($\lambda_{\rm cs}$, black). The three contours encompass 67%, 95%, and 99% of the grid cells in the reconstruction volume. The dashed lines represent the perfect relation. The fields are smoothed on a scale of $4\,h^{-1}$Mpc.

TABLE 2
UNCERTAINTIES IN THE RECONSTRUCTED DENSITY, TIDAL AND VELOCITY FIELDS AT $z = 0$

| density | $\rho_{\rm hd}$ | $\rho_{\rm cs}$ |
|---|---|---|
| $R_{\rm s} = 4\,h^{-1}$Mpc | 0.09 dex | 0.10 dex |
| $R_{\rm s} = 2\,h^{-1}$Mpc | 0.20 dex | 0.23 dex |

| tidal | $\lambda_{1,\rm hd}$ | $\lambda_{2,\rm hd}$ | $\lambda_{3,\rm hd}$ | $\lambda_{1,\rm cs}$ | $\lambda_{2,\rm cs}$ | $\lambda_{3,\rm cs}$ |
|---|---|---|---|---|---|---|
| $R_{\rm s} = 4\,h^{-1}$Mpc | 0.20 | 0.18 | 0.19 | 0.21 | 0.20 | 0.21 |
| $R_{\rm s} = 2\,h^{-1}$Mpc | 0.60 | 0.55 | 0.53 | 0.63 | 0.59 | 0.57 |

| velocity | $v_{\rm cs}$(inner) | $v_{\rm cs}$(middle) | $v_{\rm cs}$(boundary) |
|---|---|---|---|
| $R_{\rm s} = 4\,h^{-1}$Mpc | 79.9 km s$^{-1}$ | 131.9 km s$^{-1}$ | 194.7 km s$^{-1}$ |
| $R_{\rm s} = 2\,h^{-1}$Mpc | 86.5 km s$^{-1}$ | 135.7 km s$^{-1}$ | 198.5 km s$^{-1}$ |

calculated from the CS ($\lambda_{i,\rm cs}$) versus the corresponding quantities calculated directly from the MS simulation ($\lambda_{i,\rm si}$). The tidal fields are calculated using Eqs. (2) and (3), and are smoothed on the scale of $4\,h^{-1}$Mpc. Overall, $\lambda_{i,\rm cs}$ are strongly correlated with $\lambda_{i,\rm si}$, without significant bias. The typical scatter in terms of the r.m.s in $\lambda_{i,\rm si} - \lambda_{i,\rm cs}$, is around 0.2 (0.21 for the major, 0.20 for the intermediate, and 0.20 for minor axes, respectively). Adopting a smaller smoothing scale of $2\,h^{-1}$Mpc, increases the scatter to about 0.6. This increase is almost certainly due to the fact that small scale structures have significant contribution to the tidal field, but are more difficult to be constrained accurately than large scale structures.

For comparison, we also show the results for the tidal field calculated based on $\rho_{\rm hd}$. The corresponding eigenvalues $\lambda_{i,\rm hd}$ are slightly more tightly correlated with the original ones, with typical scatter of 0.20, 0.18 and 0.19 for the three axes, respectively. This shows again that the uncertainties produced by the HMC+PM is small.

Finally, we compare the velocity fields derived from the CS ($v_{\rm cs}$) with the true velocity in the original simulation ($v_{\rm si}$). Because the structures outside the reconstruction volume are unconstrained, the motion induced by these structures cannot be properly recovered by our methods. The uncertainty caused by such effect is expected to be stronger near the boundary of the reconstruction volume. To quantify this effect, we define a parameter to indicate the distance to the boundary. Following Wang et al. (2012, see also Section 2.4), we use $f_{\rm c}(R_{\rm b})$ with $R_{\rm b} = 80\,h^{-1}$Mpc to indicate the closeness of a grid to the boundary. For a grid cell close to the boundary the value of $f_{\rm c}(80\,h^{-1}{\rm Mpc})$ is expected to be smaller than one, while for a grid cell located more than $R80\,h^{-1}$Mpc away from the survey boundary, $f_{\rm c}(80\,h^{-1}{\rm Mpc}) = 1$. We divide the reconstruction volume into three parts according to the values of $f_{\rm c}(80\,h^{-1}{\rm Mpc})$ and examine them separately. Furthermore, since the mass fluctuations on scales larger than our reconstruction volume may induce a bulk motion in the whole reconstruction volume, we also subtract the mean velocity in the whole reconstruction volume from all velocities used in our calculation. Figure 22 shows $v_{\rm cs} - \bar{v}_{\rm cs}$ versus $v_{\rm si} - \bar{v}_{\rm si}$ for grid cells in the inner region ($f_{\rm c}(80\,h^{-1}{\rm Mpc}) \geq 0.8$), the intermediate region ($0.8 > f_{\rm c}(80\,h^{-1}{\rm Mpc}) \geq 0.6$) and the boundary region ($f_{\rm c}(80\,h^{-1}{\rm Mpc}) < 0.6$). Here, $v_{\rm cs}$ and $v_{\rm si}$ represent a single velocity component along one of the three axes of the Cartesian coordinates, and $\bar{v}_{\rm cs}$ and $\bar{v}_{\rm si}$ are the corresponding mean velocities in each of the $f_c$ regions (their absolute values are less than 50 km s$^{-1}$). Since the results for the three velocity components are similar, we plot them together.

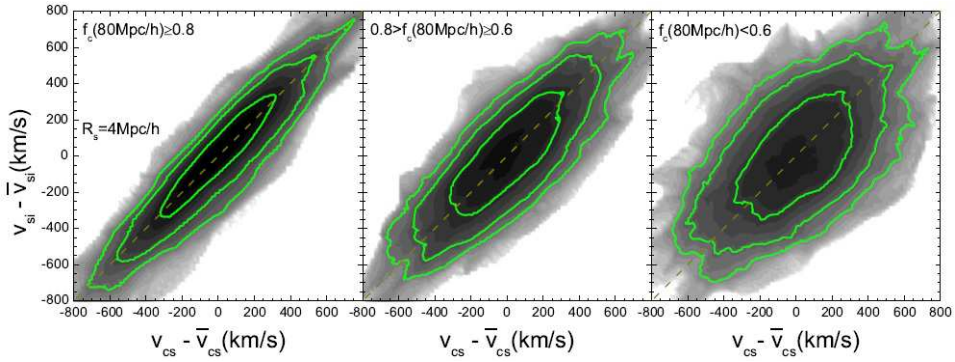


FIG. 22.— The one dimensional velocity obtained from the CS versus the velocity in the original simulation. Results are shown for grid cells with three different $f_{\rm c}(80\,h^{-1}{\rm Mpc})$, which is used to indicate the closeness to the boundary (see text for definition). The dashed lines indicate a perfect relationship. All the velocity fields are smoothed on a scale of $4\,h^{-1}$Mpc.

The velocity fields shown in the figure are smoothed with $R_{\rm s} = 4\,h^{-1}$Mpc. In the inner region, the reconstructed velocity is linearly correlated with the true velocity, with slope very close to unity. The typical scatter, in terms of r.m.s in $v_{\rm si} - v_{\rm cs}$, is about $80\,{\rm km\,s^{-1}}$. As $f_{\rm c}$ decreases, the slope remains around unity, but the scatter increases. For grid cells in the intermediate and boundary regions, the values of the scatter are 132 and $195\,{\rm km\,s^{-1}}$, respectively. When smoothed with a smaller $R_{\rm s}$ of $2\,h^{-1}$Mpc, the scatter increases only slightly to 87, 136 and $199\,{\rm km\,s^{-1}}$ for the three $f_c$ regions. Note that the volumes of the inner, intermediate and boundary regions are 45%, 31% and 24% of the total reconstruction volume, respectively.

We have also checked the dependence of the uncertainties in the density and tidal fields on $f_{\rm c}$. The uncertainties for the two quantities are found to be almost independent of the distance to the boundary so we do not show the results. Note that all of these uncertainties are estimated at $z = 0$, and listed in Table 2.

## REFERENCES


Abazajian K. N., et al., 2009, ApJS, 182, 543-558
Baldry I. K., Glazebrook K., Brinkmann J., Ivezić Ž., Lupton R. H., Nichol R. C., Szalay A. S., 2004, ApJ, 600, 681
Behroozi P. S., Conroy C., Wechsler R. H., 2010, ApJ, 717, 379
Blanton M. R., et al., 2005, AJ, 129, 2562
Brenier Y., Frisch U., Hénon M., Loeper G., Matarrese S., Mohayaee R., Sobolevskiĭ A., 2003, MNRAS, 346, 501
Briel U. G., Henry J. P., Boehringer H., 1992, A&A, 259, L31
Brown M. L., Taylor A. N., Hambly N. C., Dye S., 2002, MNRAS, 333, 501
Cooray A., Sheth R., 2002, PhR, 372, 1
Croton D. J., et al., 2006, MNRAS, 365, 11
Diemand J., Moore B., Stadel J., 2004, MNRAS, 352, 535
Danforth C. W., Shull J. M., 2008, ApJ, 679, 194-219
Davis M., Efstathiou G., Frenk C. S., White S. D. M., 1985, ApJ, 292, 371
Doumler T., Hoffman Y., Courtois H., Gottlöber S., 2013, MNRAS, 430, 888
Dunkley J., et al., 2009, ApJS, 180, 306
Enßlin T. A., Biermann P. L., Klein U., Kohle S., 1998, A&A, 332, 395
Faltenbacher A., Li C., White S. D. M., Jing Y.-P., Shu-DeMao, Wang J., 2009, RAA, 9, 41
Fitchett M., Webster R., 1987, ApJ, 317, 653
Forero-Romero J. E., Hoffman Y., Gottlöber S., Klypin A., Yepes G., 2009, MNRAS, 396, 1815
Frenk C. S., White S. D. M., 2012, AnP, 524, 507
Gao L., White S. D. M., Jenkins A., Stoehr F., Springel V., 2004, MNRAS, 355, 819
Giovannini G., Feretti L., Andernach H., 1985, A&A, 150, 302
Gott J. R., III, Jurić M., Schlegel D., Hoyle F., Vogeley M., Tegmark M., Bahcall N., Brinkmann J., 2005, ApJ, 624, 463
Guo Q., et al., 2011, MNRAS, 413, 101
Hahn O., Porciani C., Carollo C. M., Dekel A., 2007, MNRAS, 375, 489
Heß S., Kitaura F.-S., Gottlöber S., 2013, MNRAS, 435, 2065
Hockney R. W., Eastwood J. W., 1981, Computer Simulation Using Particles, New York: McGraw-Hill
Hoffman Y., Ribak E., 1991, ApJ, 380, L5
Hoffman Y., Metuki O., Yepes G., Gottlöber S., Forero-Romero J. E., Libeskind N. I., Knebe A., 2012, MNRAS, 425, 2049
Jasche J., Wandelt B. D., 2013, MNRAS, 432, 894
Jing Y. P., Mo H. J., Börner G., 1998, ApJ, 494, 1
Kaiser N., 1987, MNRAS, 227, 1
Kang X., Jing Y. P., Mo H. J., Börner G., 2005, ApJ, 631, 21
Katz N., 1992, ApJ, 391, 502
Kitaura F.-S., 2013, MNRAS, 429, L84
Klypin A., Hoffman Y., Kravtsov A. V., Gottlöber S., 2003, ApJ, 596, 19
Koribalski B. S., et al., 2004, AJ, 128, 16
Kravtsov A. V., Berlind A. A., Wechsler R. H., Klypin A. A., Gottlöber S., Allgood B., Primack J. R., 2004, ApJ, 609, 35
Lavaux G., 2010, MNRAS, 406, 1007
Lavaux G., Wandelt B. D., 2010, MNRAS, 403, 1392
Leclercq F., Lavaux G., Jasche J., Wandelt B., 2016, arXiv, arXiv:1606.06758
Li C., Kauffmann G., Jing Y. P., White S. D. M., Börner G., Cheng F. Z., 2006, MNRAS, 368, 21
Li C., Jing Y. P., Kauffmann G., Börner G., Kang X., Wang L., 2007, MNRAS, 376, 984
Lu Y., Mo H. J., Weinberg M. D., Katz N., 2011, MNRAS, 416, 1949
Lu Z., Mo H. J., Lu Y., Katz N., Weinberg M. D., van den Bosch F. C., Yang X., 2014, MNRAS, 439, 1294
Miniati F., Ryu D., Kang H., Jones T. W., 2001, ApJ, 559, 59
Mo H., van den Bosch F. C., White S., 2010, Galaxy Formation and Evolution (Cambridge: Cambride University Press).
Mo H. J., White S. D. M., 1996, MNRAS, 282, 347
Mo H. J., Yang X., van den Bosch F. C., Katz N., 2005, MNRAS, 363, 1155
Muñoz-Cuartas J. C., Müller V., Forero-Romero J. E., 2011, MNRAS, 417, 1303
Navarro J. F., White S. D. M., 1993, MNRAS, 265, 271
Navarro J. F., Frenk C. S., White S. D. M., 1997, ApJ, 490, 493
Norberg P., et al., 2001, MNRAS, 328, 64
Nusser A., Dekel A., 1992, ApJ, 391, 443
Peacock J. A., 1997, MNRAS, 284, 885
Peacock J. A., Smith R. E., 2000, MNRAS, 318, 1144
Peebles P. J. E., 1980, The large-scale structure of the universe (Princeton University Press).
Peebles P. J. E., 1989, ApJ, 344, L53
Peebles P. J. E., Nusser A., 2010, Natur, 465, 565
Peng Y.-j., et al., 2010, ApJ, 721, 193
Reed D., Gardner J., Quinn T., Stadel J., Fardal M., Lake G., Governato F., 2003, MNRAS, 346, 565
Rosati P., Borgani S., Norman C., 2002, ARA&A, 40, 539
Sanders J. S., Fabian A. C., Churazov E., Schekochihin A. A., Simionescu A., Walker S. A., Werner N., 2013, Sci, 341, 1365
Schaye J., et al., 2015, MNRAS, 446, 521
Sheth R. K., Mo H. J., Tormen G., 2001, MNRAS, 323, 1
Shi J., Wang H., Mo H. J., 2015, ApJ, 807, 37
Shi F., et al., 2016, arXiv, arXiv:1608.02313
Skrutskie M. F., et al., 2006, AJ, 131, 1163
Sorce J. G., et al., 2016, MNRAS, 455, 2078

Springel V., 2005, MNRAS, 364, 1105
Springel V., et al., 2005, Natur, 435, 629
Tully R. B., et al., 2013, AJ, 146, 86
Vale A., Ostriker J. P., 2006, MNRAS, 371, 1173
van den Bosch F. C., et al., 2007, MNRAS, 376, 841
Vogelsberger M., et al., 2014, MNRAS, 444, 1518
Wang H., Mo H. J., Jing Y. P., Guo Y., van den Bosch F. C., Yang X., 2009, MNRAS, 394, 398
Wang H., Mo H. J., Jing Y. P., Yang X., Wang Y., 2011, MNRAS, 413, 1973
Wang H., Mo H. J., Yang X., van den Bosch F. C., 2012, MNRAS, 420, 1809
Wang H., Mo H. J., Yang X., van den Bosch F. C., 2013, ApJ, 772, 63
Wang H., Mo H. J., Yang X., Jing Y. P., Lin W. P., 2014, ApJ, 794, 94, Paper I
White S. D. M., Frenk C. S., 1991, ApJ, 379, 52
White S. D. M., Rees M. J., 1978, MNRAS, 183, 341
Willick J. A., Courteau S., Faber S. M., Burstein D., Dekel A., Strauss M. A., 1997, ApJS, 109, 333
Yang X., Mo H. J., van den Bosch F. C., 2003, MNRAS, 339, 1057
Yang X., Mo H. J., Jing Y. P., van den Bosch F. C., Chu Y., 2004, MNRAS, 350, 1153
Yang X., Mo H. J., van den Bosch F. C., Jing Y. P., 2005, MNRAS, 356, 1293
Yang X., Mo H. J., van den Bosch F. C., Pasquali A., Li C., Barden M., 2007, ApJ, 671, 153
Yang X., Mo H. J., van den Bosch F. C., 2009, ApJ, 695, 900
York D. G., et al., 2000, AJ, 120, 1579
Young J. S., et al., 1995, ApJS, 98, 219
Zehavi I., et al., 2002, ApJ, 571, 172
Zehavi I., et al., 2011, ApJ, 736, 59
Zel'dovich Y. B., 1970, A&A, 5, 84
Zheng Z., et al., 2005, ApJ, 633, 791
Zhang Y., Yang X., Wang H., Wang L., Mo H. J., van den Bosch F. C., 2013, ApJ, 779, 160
Zhao D. H., Jing Y. P., Mo H. J., Börner G., 2009, ApJ, 707, 354